Chemical
Science

ROYAL SOCIETY
OF CHEMISTRY

REVIEW

View Article Online
View Journal | View Issue

Cite this: *Chem. Sci.*, 2025, **16**, 22900

# Covalent/metal–organic framework membranes with tailored pore functionality for accurate ion separation

Penglin Cheng,[a] Tiantian Chen,[b] Tiantian Liu,[a] Yuhan Wei,[a] Miaomiao Tian,*[c]
Xueli Cao,[d] Shi-Peng Sun,[d] Yatao Zhang,[a] Bart Van der Bruggen[b]
and Junyong Zhu*[a]

Ion-selective membranes present a promising solution for efficient ion extraction, a critical need addressing both water resource cycling and critical metal supplies. Conventional polymer membranes often exhibit an intrinsic permeability–selectivity trade-off, stemming from their disordered and random pore architecture. This structural limitation further complicates the understanding of how diverse ion species are transported within their non-uniform sub-nanochannels. Covalent organic frameworks (COFs) and metal–organic frameworks (MOFs) stand out as a promising solution for ion separation due to their ordered pore architecture, designable topological configuration, and tunable pore microenvironment. Herein, recent advancements in ion-selective membranes fabricated using these advanced COF and MOF materials are critically reviewed. We begin by unravelling the currently dominant ion-differentiation mechanisms within their sub-nanochannels, including size exclusion, electrostatic interactions, and chemically specific binding. Particular emphasis is placed on the pore engineering design principles of these crystalline framework materials, highlighting the role of specific ion-binding moieties, pore dimensions and charge, and asymmetric structures in selective ion transport. Advanced fabrication methods and ion-related applications of crystalline framework-based membranes are subsequently described. We conclude by presenting fundamental prospects and challenges for the on-demand design of next-generation ion-selective framework membranes.

Received 18th September 2025
Accepted 16th November 2025

DOI: 10.1039/d5sc07238g

rsc.li/chemical-science

## 1 Introduction

The global proliferation of industries in the petrochemical, tannery, and textile sectors has precipitated the discharge of significant volumes of saline wastewater.[1–3] Among the diverse array of contaminants, heavy metal ions are of particular concern given their pronounced tendency toward bioaccumulation in biological organisms, leading to compromised immune function and disrupted metabolic pathways.[4–8] Conversely, the parallel expansion of burgeoning industries—including new energy, precision manufacturing, and smart technologies—has driven a soaring demand for various critical ions (*e.g.*, lithium and rare earth metals).[9–12] Consequently, the efficient extraction and recovery of these valuable ionic resource species from unconventional sources (*e.g.*, salt lakes and industrial effluents) not only mitigates the global environmental crisis and resource scarcity but also actively facilitates a circular economy.[13–17] Nonetheless, high-value ionic species within natural or secondary sources are frequently dilute and intermixed with coexisting entities of similar size and charge. This presents a formidable obstacle to their selective extraction and concomitantly escalates associated processing expenditures. On the other hand, traditional separation techniques inherently suffer from the inefficient recovery of target species alongside compromised product purity stemming from interference by co-existing ions. Furthermore, the requisite introduction of chemical reagents and the reliance on energy-intensive separation processes lead to additional environmental burdens.[18] In this context, there is an urgent need for the development of advanced separation technologies that enable precise and sustainable ion separation.

Membranes function as thin, selectively permeable barriers designed for the separation of mixtures by allowing the passage of specific target substances while rejecting competitive ones. This separation is achieved through diverse driving forces: concentration differences (pervaporation),[19] pressure gradients (nanofiltration (NF) and reverse osmosis (RO)),[20,21] or potential

---

[a] *School of Chemical Engineering, Zhengzhou University, Zhengzhou, 450001, P. R. China. E-mail: zhujunyong@zzu.edu.cn*

[b] *Department of Chemical Engineering, KU Leuven, Celestijnenlaan 200F, B-3001, Leuven, Belgium*

[c] *School of Ecology and Environment, Zhengzhou University, Zhengzhou, 450001, P. R. China. E-mail: tianmiaomiao@zzu.edu.cn*

[d] *NJTECH University Suzhou Future Membrane Technology Innovation Center, Suzhou, 215100, China*

differences (electrodialysis, ED).[22] Membrane-based separations offer a promising avenue for ion separation, attributable to their facile continuous operation, high energy efficiency, and small environmental footprint. They have significant potential to promote the circular economy and optimize the industrial structure.[23] To date, techniques like NF, RO, and ED have achieved considerable maturity in applications in seawater desalination,[24,25] heavy metal removal,[26,27] lithium extraction,[28,29] and rare earth element separation.[30,31] Traditional ion-selective membranes are fabricated from organic polymers, such as polyamides,[32] polyimides,[33] and polyesters.[34] The exceptional stability and robust mechanical strength of these materials confer substantial benefits for commercial applications. However, amorphous polymers like polyamides generally have charged surfaces, which can lead to inorganic fouling and biofouling during separation processes. Moreover, the inherent size disparities among different ion species typically manifest at the Ångström level. Their heterogeneous pore size distribution characteristics face a critical challenge in differentiating these similarly sized ion species and thus impose a stringent selectivity/permeability trade-off. Therefore, the rational design of ion-selective membranes requires on-demand customization of membrane structures, coupled with clarification of the principles governing how structures affect separation performance, to enhance ion separation processes.

Driven by continuous advancements in reticular chemistry,[35,36] dynamic covalent chemistry,[37–39] and computational chemistry,[40] porous crystalline framework (*e.g.*, covalent organic framework: COF, and metal–organic framework: MOF) membranes have undergone rapid and significant development. COFs, synthesized through the reversible reaction of organic building blocks, represent a prevalent class of structurally well-defined, chemically rigid materials featuring permanent, long-range ordered nanochannels.[41–43] The tunable building block design of COF membranes enables on-demand synthesis and regulation of precise pore structure. This allows fine-tuning of energy barriers for transmembrane ion transport through the strategic leverage of steric hindrance, electrostatic interactions, ion–ion interactions, coordination bonds, and hydrogen bonds. A clear example is the integration of crown ethers within COF channels, which selectively facilitates metal ion transport *via* specific host–guest interactions.[44] Furthermore, post-synthetic modification strategies confer structural adaptability to COF intrinsic pores, enabling the creation of tailored pore architecture and functionality for differential transport behavior between target and competing ions. Illustratively, manipulating the positive charge density within COF nanochannels can enrich counterions that actively interact with lithium ions to mitigate dehydration energy barriers, thereby boosting their transport rates.[45] Unlike the entirely organic constitution of COFs, MOFs are periodic porous materials precisely assembled from metal ions/metal–oxo clusters and organic linkers *via* diverse coordination bonds.[46,47] These frameworks distinguish themselves by featuring large surface areas relative to conventional porous materials, underpinning their broad utility in fields like adsorption,[48] $CO_2$ capture,[49] catalysis,[50] sensing,[51] and drug delivery.[52] Notably, the bimodal pore structure of MOFs—comprising smaller windows for selectivity and larger cavities for permeability—confers distinct advantages in accurate ion separation. Inspired by the Ångström-scale asymmetric cavities of biological ion channels, Abdollahzadeh *et al.* pioneered the design of a uniquely bilayer MOF membrane. This design introduces energy barriers *via* window-size disparities between the two MOF layers, achieving remarkable $K^+/Li^+$ and $Na^+/Li^+$ selectivity of 84 and 80, respectively.[53]

This review critically examines the dominant mechanisms governing differential ion transport within sub-nanometer channels, including size exclusion relative to the dehydration effect,[54–56] electrostatic interactions,[57] and non-electrostatic interactions (coordination bonds),[58] all of which synergistically modulate ion migration (Fig. 1a). We provide a systematic overview of design principles for COF/MOF membranes, specifically addressing building block engineering, post-synthetic modification, pore size modulation, along with synthetic strategies for precisely tuning MOF apertures. Membrane fabrication approaches like *in situ* growth, secondary growth, interfacial polymerization, counter-diffusion, and layer-by-layer assembly are also afforded particular attention. Furthermore, we categorize the detailed applications of COF/MOF membranes in heavy metal removal, lithium extraction, and rare earth element separation (Fig. 1b). Furthermore, this review focuses on the cutting-edge advancements in a new generation of framework-based membranes. Specifically, it encompasses developments in stimuli-responsive smart membranes, the bio-inspired design of sub-nanometer channels, and the precise assembly of heterogeneously charged channels. These methodologies collectively provide comprehensive guidance for the design and fabrication of advanced ion-selective membranes and for the fundamental exploration of ion transport mechanisms in nano-confined environments. Importantly, discussions on thin-film nanocomposite (TFN) and mixed-matrix membranes incorporating COFs/MOFs for ion sieving are excluded here to focus exclusively on pure framework membrane performance.[59–61] Finally, we outline the key challenges and opportunities in designing next-generation framework membranes with enhanced selectivity and multifunctionality on demand.

## 2 Ion separation mechanism

Understanding ion separation mechanisms is pivotal for developing high-performance ion-selective membranes. In confined micro-channels, ion transport is governed by three crucial mechanisms: (i) size-sieving effects, (ii) electrostatic interactions, and (iii) chemical interactions. These mechanisms operate synergistically to dictate the separation performance of COF/MOF membranes.

### 2.1 Size exclusion based on steric hindrance

Steric hindrance is a pivotal determinant in transmembrane ion transport, rendering channel dimensions and shape core aspects for efficient membrane-based ion separation.[62] Yang

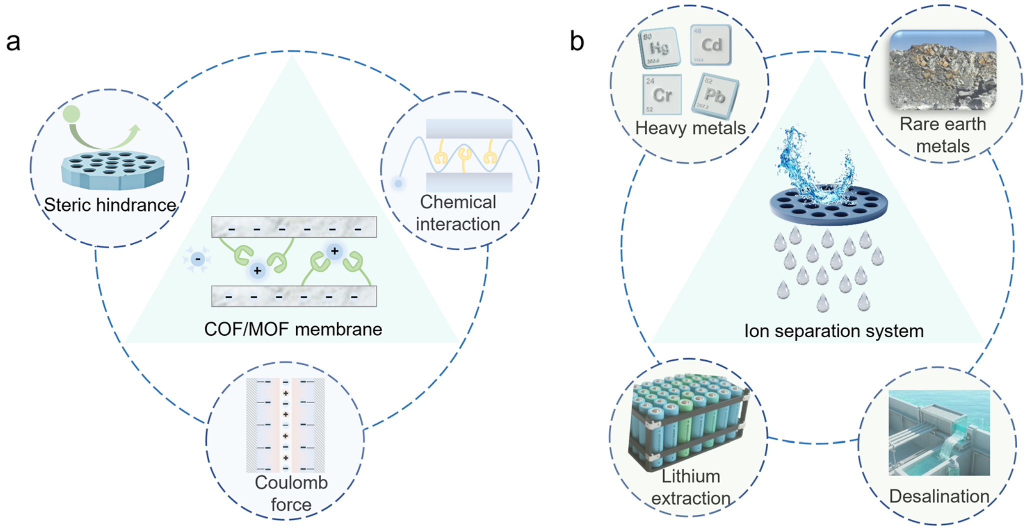

**Fig. 1** Schematic of ion-sieving mechanisms and representative applications of COF/MOF membranes. (a) Ion-sieving mechanisms of COF/MOF membranes. (b) Ion separation systems of COF/MOF membranes.

*et al.* exemplified this by developing 4-carboxyl-quinoline-linked COFs *via* Doebner reactions.[63] Their work revealed distinct cation migration within COF channels: endowed with a 14 Å pore diameter, the membrane readily transports $Hex_4N^+$ (13.4 Å) while effectively blocking $Oct_4N^+$ (17.8 Å). This size-exclusion phenomenon directly impacted conductivity, with $Hex_4N^+$ exhibiting a conductivity 2.1 times higher than that of $Dodec_4N^+$, highlighting the exquisite control over ion transport achievable through precise pore engineering.

The transport behavior of metal ions in solution is governed not by their bare ionic diameter, but by their effective hydrated radius. In aqueous environments, metal ions are surrounded by water molecules, forming a hydration shell. The extent of this hydration is fundamentally related to the ion's charge density. Higher charge density ions (*e.g.*, those with a small bare radius or high charge) strongly polarize surrounding water molecules, leading to a tightly bound, larger hydration shell and thus a greater effective hydrated radius. In contrast, lower charge density ions (*e.g.*, those with a large bare radius or low charge) induce weaker polarization, giving rise to a looser, smaller hydration shell and a correspondingly smaller effective hydrated radius.[55,64] This principle is clearly illustrated by alkali metal ions, whose effective hydrated radii increase with decreasing bare ionic radius ($Li^+ > Na^+ > K^+ > Rb^+$).[65]

Apart from steric hindrance, differences in metal ion hydration energies largely affect transmembrane ion transport. The dehydration-induced entropic gain serves to partially mitigate the enthalpic penalty associated with overcoming these hydration energies, thereby acting as a critical determinant of ion selectivity. Specifically, for metal ions possessing hydrated radii exceeding the pore dimensions, dehydration is imperative prior to channel ingress. For instance, elevated hydration energy signifies intensified ion–water interactions, rendering dehydration more difficult and imposing a higher energetic barrier for entry.[64,66]

Quantitative analysis of the hydration number distribution of metal ions within sub-nanometer channels *via in situ* liquid time-of-flight secondary ion mass spectrometry provides critical insights into the dehydration-mediated ion transport mechanism within confined spaces (Fig. 2a).[55] Owing to their smaller bare ionic radii, lithium and sodium ions permeating constricted pathways within the membrane undergo only partial dehydration. This results in a reduced average hydration number, with smaller hydrated species predominating (Fig. 2b and c). Ion transmembrane transport can be decoupled into three distinct stages: (i) partial dehydration of hydrated ions at the feed-side and their subsequent partitioning into the pore channels, (ii) rapid diffusion of metal ions through sub-nanometer channels, and (iii) desorption of metal ions at the rear end of sub-nanometer channels.[67–70]

To delineate the underlying mechanisms governing ion transport within UiO-67 membranes, Xu *et al.* conducted temperature-dependent ionic conductivity measurements on $Li^+$ and $Mg^{2+}$ in 0.1 M electrolyte (pH 6.3). This yielded activation energies for lithium and magnesium ion transport of 2.14 and 17.23 kcal mol$^{-1}$, respectively (Fig. 3a).[71] Meanwhile, radial distribution function (RDF) analysis was utilized to characterize the spatial distribution of water molecules surrounding metal ions at discrete locations within the UiO-67 framework. This revealed differential dehydration behavior of metal ions during their passage through the membrane windows (Fig. 3b and c). Specifically, the partial dehydration of $Li^+$ necessitates shedding only 0.9 water molecules from its second hydration shell. In contrast, $Mg^{2+}$ requires the removal of 4.6 water molecules from its second shell, thereby resulting in a significantly higher diffusion resistance (Fig. 3d). This work underlines that the UiO-67/AAO membrane features a bimodal pore architecture that comprises sub-nanometer windows and nano-cavities, which induces a repeated dehydration–hydration process during ion

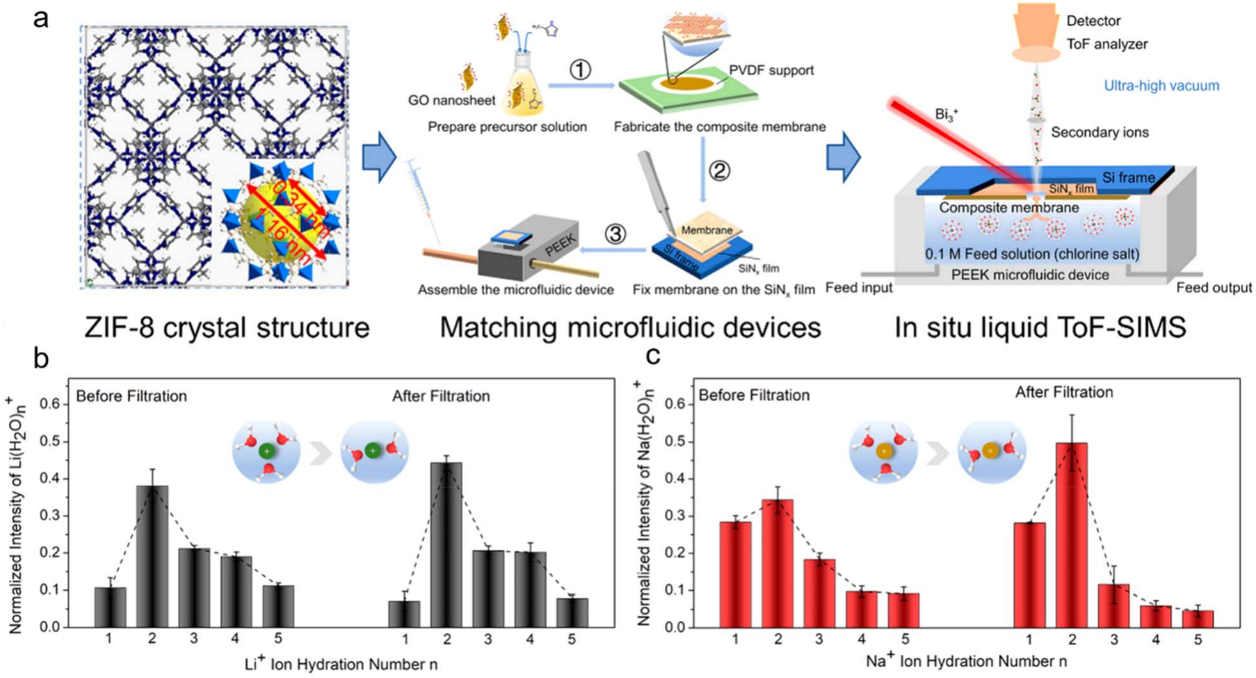

Fig. 2 Hydration structure characterization. (a) Schematic of the ZIF-8 structure and microfluidic technology coupled with *in situ* liquid ToF-SIMS analysis. The hydration structure of (b) $Li^+$ and (c) $Na^+$ before and after filtration.[55] Copyright 2023, American Chemical Society.

transport (Fig. 3e). In this process, ions undergoing extensive dehydration require substantially higher activation energies for transmembrane transport, resulting in lower kinetics. Therefore, the dehydration effect plays a critical role in the differential transport behavior of various metal ions. Furthermore, the superior selectivity of biological ion channels correlates with dehydration effects. Potassium ions, for instance, undergo substantial dehydration, enabling their passage as largely bare ions driven by coulombic collision.[72] Conversely, sodium ions typically engage in co-transport with their hydration water, which accounts for their distinct transport dynamics.

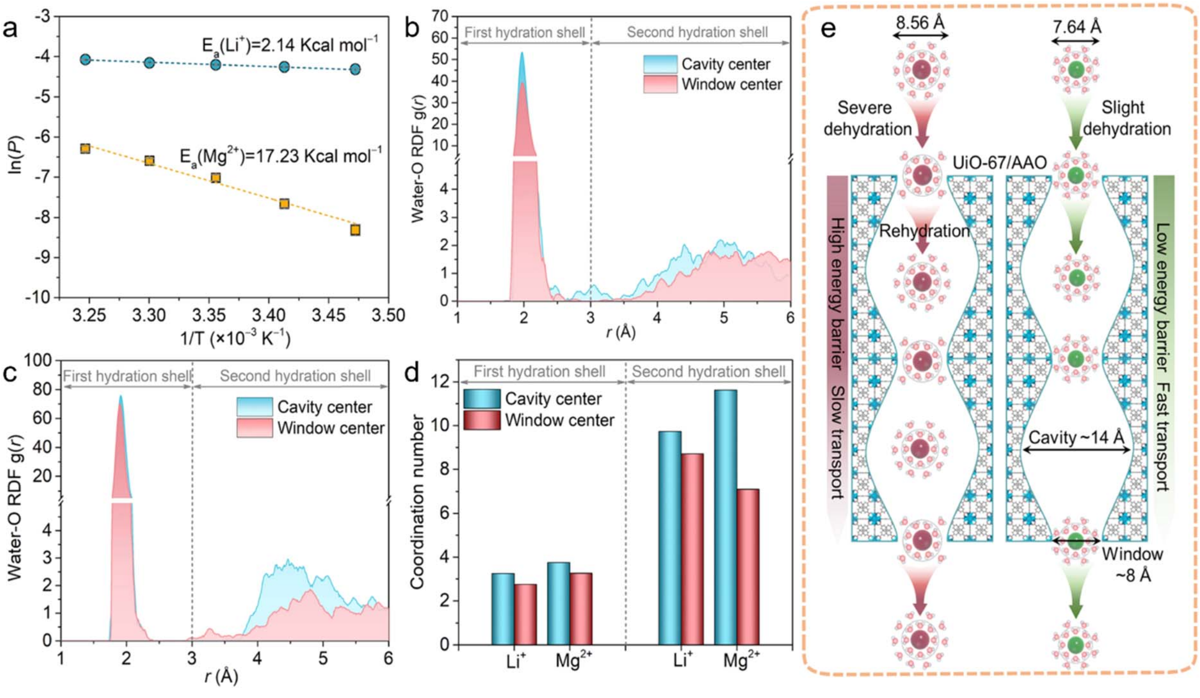

Fig. 3 Mechanistic insights into $Li^+/Mg^{2+}$ separation. (a) Ionic conductivity experiments. RDFs for (b) $Li^+$ and (c) $Mg^{2+}$ positioned at both cavity and window centers of UiO-67. (d) First and second hydration shells of $Li^+$ and $Mg^{2+}$ at diverse channel positions. (e) Proposed mechanism for $Li^+$ and $Mg^{2+}$ transport.[71] Copyright 2021, Wiley-VCH.

In addition to intrinsic pore dimensions, both experimental and computational results demonstrate that the effective cut-off size of COF membranes is correlated with the chemical environment of their pore wall. Specific functional groups lining the channels engage in strong interactions with water molecules through coordination and coulombic forces. These interactions can effectively narrow the nanochannels, thereby significantly impeding ion transport. As an exemplary case, Liu *et al.* utilized a quaternary ammonium-functionalized aldehyde monomer (HBAB) to develop a novel strategy for fabricating COF membranes featuring asymmetric architectures.[73] Specifically, the observed variation in activation energies for transmembrane ion transport within the COF membrane aligns with the sequence of both permeation rates and hydrated ionic sizes (Fig. 4a). A critical finding is that this COF membrane exhibits an effective cut-off size of 8.2 Å, with a marked reduction from its intrinsic pore size of 1.2 nm, highlighting the crucial role of the chemical environment of the pore (Fig. 4b). Consequently, these membranes enable remarkable discrimination of rare earth elements, exhibiting outstanding water fluxes of 225.4 mol m$^{-1}$ h$^{-1}$ and a high Cs$^+$/La$^{3+}$ selectivity of up to 75.9 (Fig. 4c and d). RDF indicates that the N$^+$ in the quaternary ammonium motif electrostatically binds to the electronegative oxygen atoms of water molecules, forming a localized 4.3 Å hydration layer (Fig. 4e). Metal ion transport within the sub-nanometer channels is mainly impacted by the synergistic interplay between the localized hydration layers and the electrostatic repulsion generated by the quaternary ammonium motifs. This selective transport is achieved by precisely tuning the pore aperture of COF membranes to 8 Å, a size that matches the hydrated size of La$^{3+}$ *versus* that of Cs$^+$ (Fig. 4f).

Wang *et al.* developed a novel strategy to enhance the selective separation of monovalent cations by incorporating sulfonic, phosphoric, and formic acid functionalities into COF membranes.[74] RDF analysis was employed to elucidate the influence of the hydration layer on their pore structure. The results revealed that hydrogen atoms within the COF exhibit closer proximity to water molecules compared to oxygen atoms, indicative of hydrogen bonding formation between active sites and water molecules (Fig. 5a and b). A comparative study of water molecules associated with different acidic groups demonstrated that more hydrophilic functionalities lead to the formation of thicker hydration layers. A comparison of the jump-to-contact distances (h) in atomic force microscopy (AFM) force–distance measurements established a clear sequence for the thickness of the confined water layer: TpPa-SO$_3$H > TpPa-PO$_3$H$_2$> TpPa-CO$_2$H (Fig. 5c and d). Concurrently, fitting the dielectric spectra with the Havriliak–Negami relaxation model identified a second Havriliak–Negami term in the TpPa-SO$_3$H membrane, attributable to the presence of a distinct secondary hydration layer (Fig. 5e). The effective size of the TpPa-PO$_3$H membrane was approximately 7.0 Å, which lies between the hydration diameters of K$^+$ (6.6 Å) and Li$^+$ (7.6 Å), yielding a K$^+$/Li$^+$ selectivity of 13.7.

## 2.2 Electrostatic interaction

Electrostatic interaction, serving as an important factor, affects ionic transport.[75] Compared to the bulk phase, deviations in transport behavior within the charged channels were found

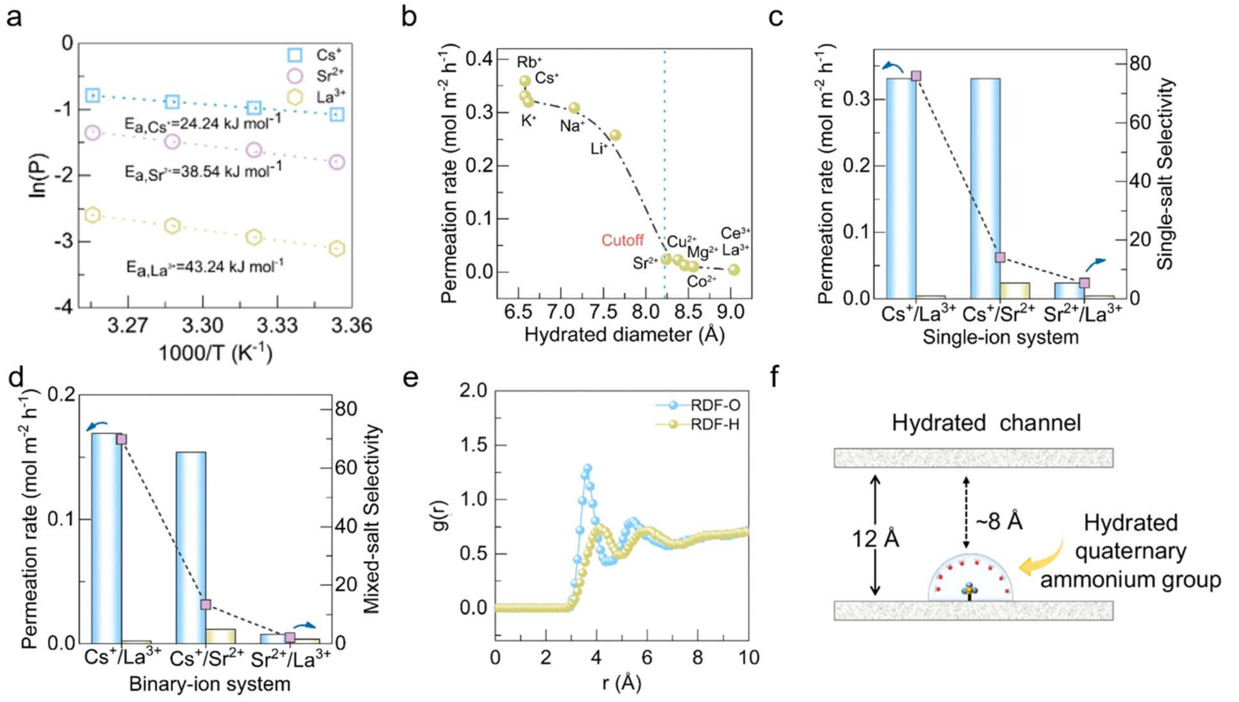

Fig. 4 Hydration layer impact on architecture and separation performance. (a) Ionic conductivity experiments. (b) Ion permeation rates. Rare earth element ion selectivity in (c) single-salt and (d) mixed-salt. (e) RDF of water molecules surrounding the quaternary ammonium units. (f) Schematic of effective pore size.[73] Copyright 2024, Springer.

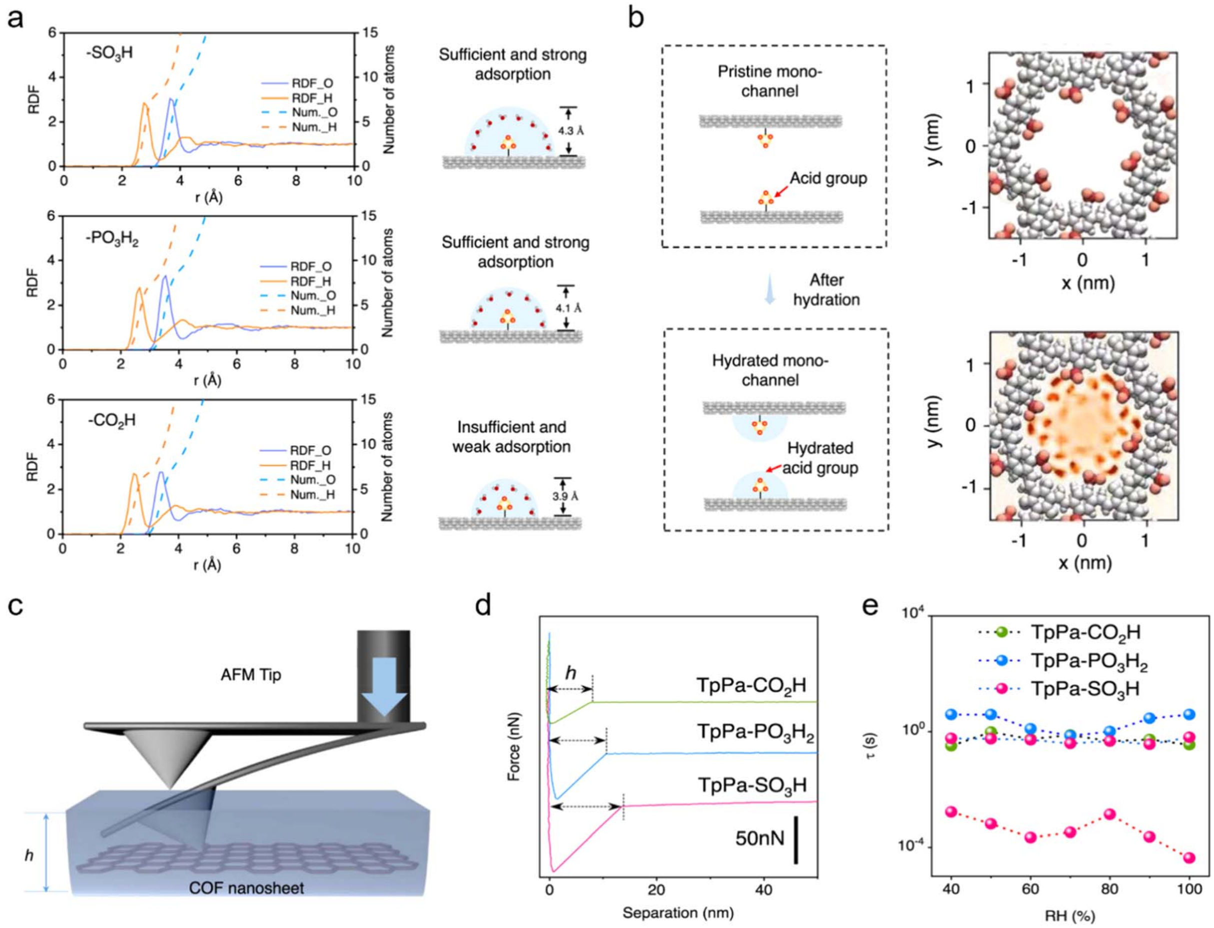

Fig. 5 Functionality impact on hydration layer thickness. (a) RDF of water molecules surrounding acidic groups. (b) Schematic of hydration layer impact on the structure of COF channels. (c) Schematic of contact AFM measurement and its corresponding "jump-to-contact" region. (d) Force–distance curve. (e) Dielectric loss spectra.[74] Copyright 2022, Springer.

when conducting ionic conductivity experiments with KCl as the electrolyte. This demonstrated that, in addition to size exclusion, long-range coulombic interactions with charged functional groups in the membrane can effectively discriminate metal ions with distinct charges. Meanwhile, the optimized charge density enables superior separation selectivity without sacrificing water permeability.[57] Specifically, electrostatic interactions critically govern migration dynamics and interfacial phenomena of mono-/multivalent ions. For example, surface fixed charges in polyamide membranes suppress co-ion partitioning through electrostatic exclusion. However, fixed internal charges facilitate accelerated co-ion diffusion *via* electrostatic attraction.[76] Consequently, during the transmembrane transport of ions, the permeation rate of co-ions is inhibited, and the energy barrier rises. Conversely, counter-ions show facilitated diffusion rates and reduced energetic penalties. It is worth noting that the disordered arrangement of charged moieties in crosslinked networks of traditional polymeric membranes often impairs electrostatically-mediated separation processes. This structural irregularity further complicates mechanistic investigations into how electrostatic interactions regulate ion transport within confined spaces. In contrast, the inherent long-range order and customizable periodic porous architecture of COF/MOF membranes provide precisely engineered charged channels. This unique structural control facilitates rigorous mechanistic studies on ion-charged channel interactions and confined transport phenomena at the molecular level.

Leveraging the tailorable pore architectures of COFs, Hou *et al.* engineered intrinsic nanochannels with fine-tuned charge densities to decouple the role of electrostatic interactions in ion transport (Fig. 6a).[57] The results revealed that magnesium ion permeation was progressively inhibited with an increase in membrane charge density. Beyond a critical threshold, however, the augmented charged motifs on pore walls induced a pronounced enrichment of counterions ($Cl^-$), thereby leading to enhanced transport of magnesium ions. You *et al.* conducted a comparative study on the separation performance of an ionic COF membrane and a commercial membrane, specifically investigating the impact of charged nanochannels on transport behavior.[77] The ionic COF membrane exhibited unexpectedly lower rejection of $MgCl_2$ in comparison to NaCl. This observation deviates from predictions based solely on conventional size-mediated membrane separation mechanisms (Fig. 6b and

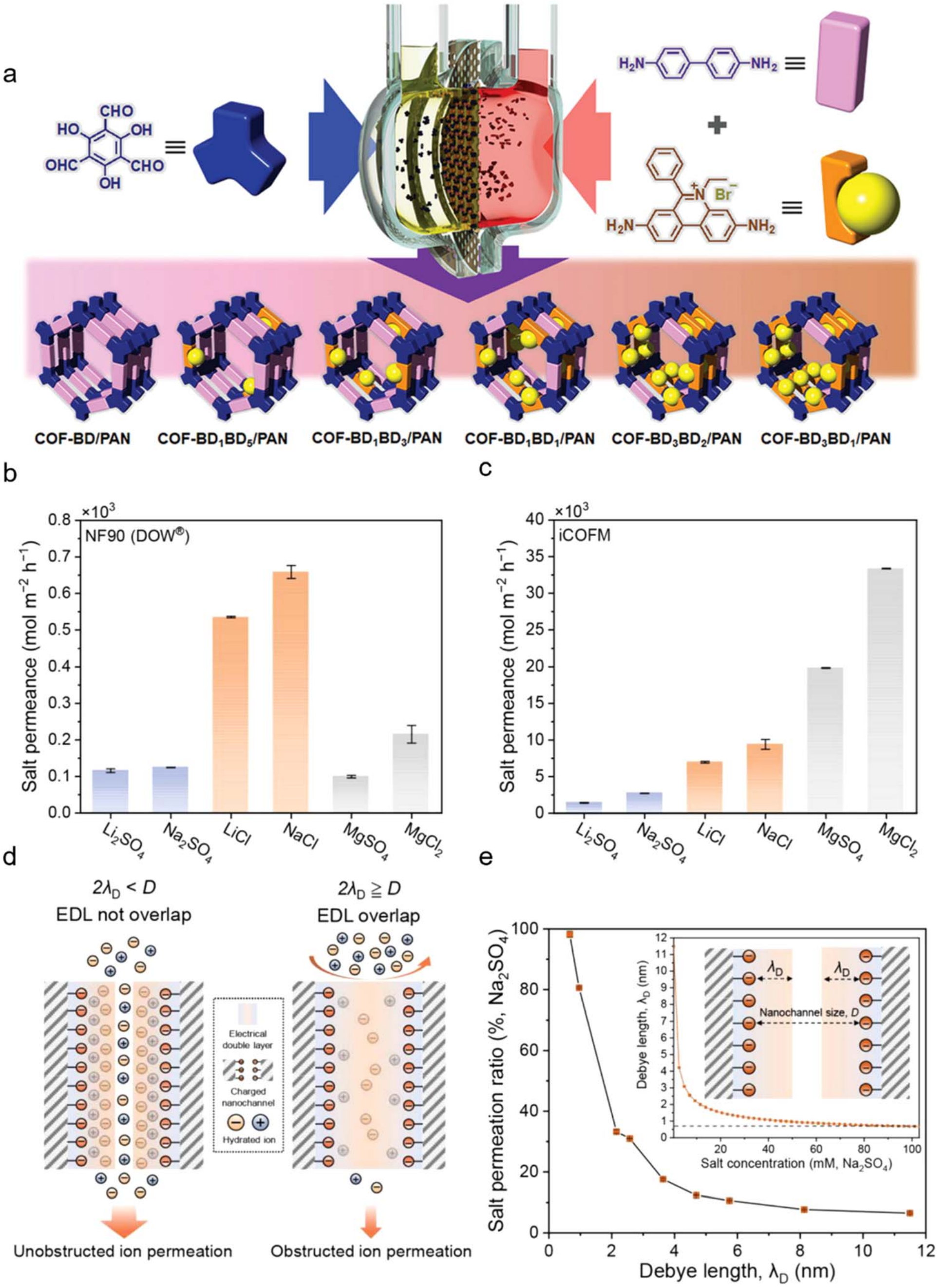

Fig. 6 (a) Schematic of charge density modulation through precise monomer ratio control.[57] Copyright 2021, Wiley-VCH. Ion transport behavior governed by the electric double-layer. Salt permeation rates of (b) commercial nanofiltration membranes *versus* (c) ionic COF membranes. (d) Electric double layer-governed ion diffusion behavior. (e) Salt permeability at varying Debye lengths. Insets: illustration of the Debye length–salt concentration correlation.[77] Copyright 2022, American Chemical Society.

c). The underlying principle is explained by the electric double layer (EDL) theory, which posits that counterions within electrolyte solutions accumulate near charged surfaces due to coulombic interactions, thereby promoting the screening of electrostatic potentials. The characteristic thickness of this accumulated counterion layer is known as the Debye length ($\lambda_D$). When $\lambda_D$ exceeds the pore radius, EDL overlap occurs, which directly enables the charge distribution within the nanochannels to become the dominant factor governing ion transport behavior (Fig. 6d). Counterions with higher valence possess an enhanced capability to neutralize pore charges, consequently reducing the Debye length. This explains the observed lower rejection of $MgCl_2$ compared to NaCl. Given that the Debye length is inversely correlated with electrolyte concentration, and salt permeability itself is inversely proportional to $\lambda_D$, an increase in salt concentration consequently leads to a decrease in salt rejection (Fig. 6e).

Heterogeneous architecture represents a fascinating aspect of biomimetic membrane design, creating unprecedented opportunities to break performance limits and construct multifunctional materials. Notably, the asymmetric distribution of charged groups, a representative heterostructure design, precisely modulates the ion partitioning–diffusion process. Considering metal cations, for example, negatively charged channels with a relatively strong electrostatic affinity promote the partitioning of these ions into the pore channels, lowering the energy barrier for ion entry. Conversely, this same electrostatic interaction concurrently leads to an increased energy barrier for ion egress from the channels. Homogeneously charged channels therefore impede rapid ion permeation, whereas heterogeneous charge architectures demonstrate remarkable potential for facilitating transport. Xu *et al.* developed a heterogeneously charged COF membrane by finely controlling the polycation distribution.[70] This engineered channel structure was conceptualized as three sequential segments: a negatively charged entrance, a weakly charged intermediate region, and a positively charged exit (Fig. 7a). The precise introduction of polyelectrolytes within the membrane established an internal micro-electric field, which specifically facilitates $Li^+$ permeation. Quantitative analysis *via* mean squared displacement (MSD) corroborated this, demonstrating preferential $Li^+$ transport through relative displacement quantification (Fig. 7b). The negative entrance functions as a "cation receptor", facilitating the capture of cations into the channel (Fig. 7c). Subsequently, the weakly charged inner region mitigates ion-channel friction, thereby augmenting ion migration kinetics and reducing the overall interaction energy (Fig. 7d). Finally, the positive charge at the exit significantly lowers the energy barrier for $Li^+$ from the channel (Fig. 7e). This heterogeneously charged distribution is conductive to the transfer of lithium, yielding a high $Li^+/Mg^{2+}$ selectivity of 61.6.

A compelling demonstration of selective mono-/divalent ion separation was provided by Lu *et al.* through their innovative design of metal–organic framework (MOF) sub-nanochannels, specifically using UiO-66-$(COOH)_2$.[78] Molecular simulations revealed that this selectivity arises from two concurrent processes: partial dehydration of metal ions during their passage through MOF-windows and their subsequent electrostatic interactions with MOF carboxyl groups. Specifically, divalent ions exhibited stronger binding affinity and higher diffusion barriers within the channels. This, coupled with their elevated dehydration energy barriers stemming from higher charge density, collectively enables superior mono-/divalent ion selectivity.

Within sub-nanometer channels, ion–pore interactions are significantly mediated by the dynamics of hydration layers. During the adsorption/partitioning process from the feed side, hydrated ions exhibit differential dehydration behaviors. The stripping of hydration shells largely boosts electrostatic interactions between the ions and the membrane. Specifically, a higher degree of dehydration exposes more effective ionic charge, leading to stronger electrostatic forces.[79] Alternatively, it is recognized that electrostatic interactions within sub-nanometer channels promote the dehydration of counter-ions.[80–82] This phenomenon affects the partitioning behavior of co-ions at the channel entrance. Conversely, the electrostatic

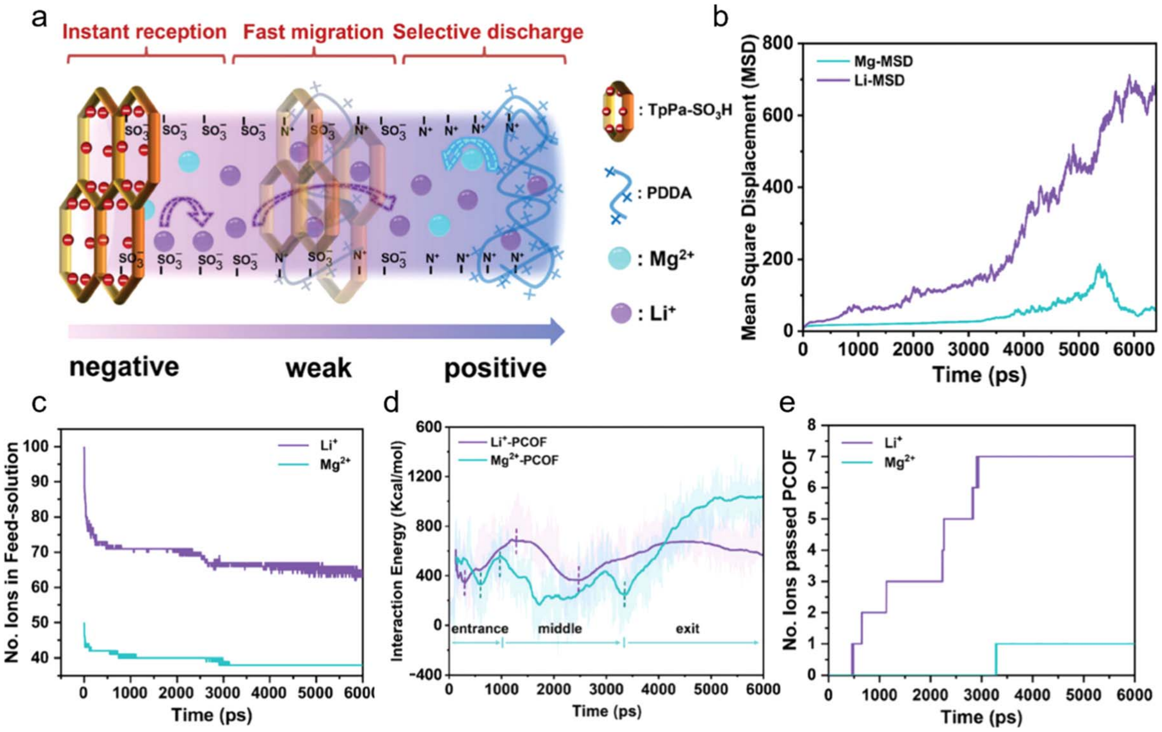

Fig. 7 Lithium–magnesium separation in heterocharged COF membranes. (a) Schematic of heterocharged nanochannels. (b) MSD of $Mg^{2+}/Li^+$. (c) Quantity of $Li^+$ and $Mg^{2+}$ in feed-solution. (d) Binding energy between ions and the COF. (e) Ion transport numbers across COFs.[70] Copyright 2024, Wiley-VCH.

repulsion of co-ions by the channel walls stabilizes their hydrated structure, and this resulting larger hydrated size hinders their partitioning into the entrance.

### 2.3 Chemical interaction

Conventional membranes achieve ion separation primarily through size sieving, excluding ions larger than the pore size, and electrostatic repulsion for similarly charged species. This dual mechanism, however, severely restricts their selectivity towards coexisting ions with comparable charge properties and dimensions.[83,84] Inspired by biological ion channels, which are crucial for maintaining physiological processes, researchers have recently focused on achieving high-precision ion separation based on coordination interactions. Specifically, quantum chemistry reveals that a coordination interaction forms when a ligand donates a lone pair of electrons to an unoccupied orbital of another atom or ion. This coordination behavior allows significant differentiation between metal ions, even those with similar dimensions and charge characteristics. For instance, alkali metal ions exhibit distinct coordination behaviors with ligands due to their varying electronic configurations. Ligand field theory explains this by showing that minimized electronic repulsion, achieved when functional group orbitals complement those of the ions, results in lower energy states and favorable coordination bond formation. A key example is polymeric membranes, where incorporated functional groups with preferential binding affinity towards target ions govern transport based on binding energetics, rather than solely on membrane thickness.[85] Given that these atomic-level interactions, explored in quantum chemistry, are primarily applicable at the Ångström level, the development of Ångström-level COF/MOF channels and the strategic incorporation of metal-ion-recognizing groups in COF/MOF membrane design hold significant promise for achieving high-precision and universal ion separation.

Lithium ions, due to their small ionic radius and high charge density, demonstrate a strong propensity to form coordination bonds with the lone pair electrons of oxygen atoms, as observed in crown ethers.[33,86,87] Inspired by this fundamental understanding, Bing *et al.* engineered ion-selective membranes by incorporating oligoether into 2D COFs (Fig. 8a and b).[88] To elucidate the impact of side oligoether groups, the synthesis of COFs with precisely controlled pore sizes and chemical environments was achieved by introducing specific side chains at the *ortho*-position of the aldehyde group (Fig. 8c). Their findings elucidated a crucial mechanism: oligoethers significantly reduce transmembrane barriers for lithium ions by displacing water molecules from their hydration shell, thereby mitigating the associated dehydration energy penalties. In contrast, the robust hydration shells of magnesium ions impede their transport. DFT calculations further demonstrated that oxygen atoms within oligoethers form stable coordination with $Li^+$, exhibiting a markedly higher binding affinity compared to competing ions. Furthermore, their chain flexibility enabled rapid coordination–dissociation dynamics with $Li^+$, facilitating ion migration though a relay mechanism. This strategic incorporation of lithophilic oligoethers into the COF channels facilitates the transfer of lithium ions while restricting the diffusion of magnesium ions, thereby achieving a high $Li^+/Mg^{2+}$ separation factor of 64.

The selective partitioning of hydrated ions at the channel entrance is a key factor in ion migration. This process necessitates metal ions to surmount entry energy barriers, particularly those associated with partial dehydration. As a result, designing ultra-selective ion separation membranes must prioritize target ion binding, ensuring that such binding provides energetic compensation for dehydration *via* compensatory interactions. This promotes target ion partitioning or adsorption, thereby augmenting their distribution within sub-nanometer channels. However, a delicate balance is required: while insufficient affinity fails to promote target ion partitioning, excessive affinity can inadvertently elevate the ion exit energy barrier. Consequently, precise quantification of functional group-ion binding energies is paramount for engineering coordination-based ion-selective membranes.

Beyond binding, efficient transport is also crucial. Studies demonstrate that introducing binding sites within the long-range ordered channels of MOFs/COFs enables ion hopping, reducing transport energy barriers and elevating conduction rates.[89] However, introducing specific functional groups does not guarantee improved target ion transport efficiency. For example, optimal inter-site distances are essential; distances below a certain threshold facilitate ion surface hopping, whereas excessive spacing creates unfavorable energy wells for ion diffusion. This explains why the randomly distributed active sites in amorphous regions of polymeric membranes are detrimental to enhancing ion permeation. Fortunately, the emergence of COF/MOF materials with their inherent long-range ordered nanochannels offers a compelling solution, having significantly revitalized the development of advanced ion-separation membranes.

Recently, designing membrane materials that can respond to external stimuli (*e.g.*, temperature, humidity, light, and pH) was found to be highly efficient for extracting scarce ion resources.[90] Engineering smart membranes necessitates the integration of functional units for reversible physicochemical switching when exposed to external stimuli. These units primarily encompass pH-responsive moieties—such as carboxyl, phosphate, amine, and pyridine groups—which facilitate these changes by undergoing protonation or deprotonation upon pH variation. For instance, Cao *et al.* functionalized the COF intrinsic channels with cysteine, which features terminal amine and carboxyl groups as pH-responsive binding sites (Fig. 9a).[91] Specifically, the acid-induced protonated amine groups with positive charges exhibited weak interactions with metal ions, leading to the preferential transport of $K^+$ ions dominated by diffusion effects. Conversely, under alkaline conditions, the deprotonated, negatively charged carboxyl groups exhibited strong coordination interactions with metal cations, particularly favoring $Na^+$ ion transport (Fig. 9b and c). To elaborate this interaction between ions and cysteine moieties, RDF describes dual ion shells formed by $Na^+$ and $K^+$ around carboxylate groups (Fig. 9d). Evidently, $Na^+$–carboxylate pairs exhibited narrow and

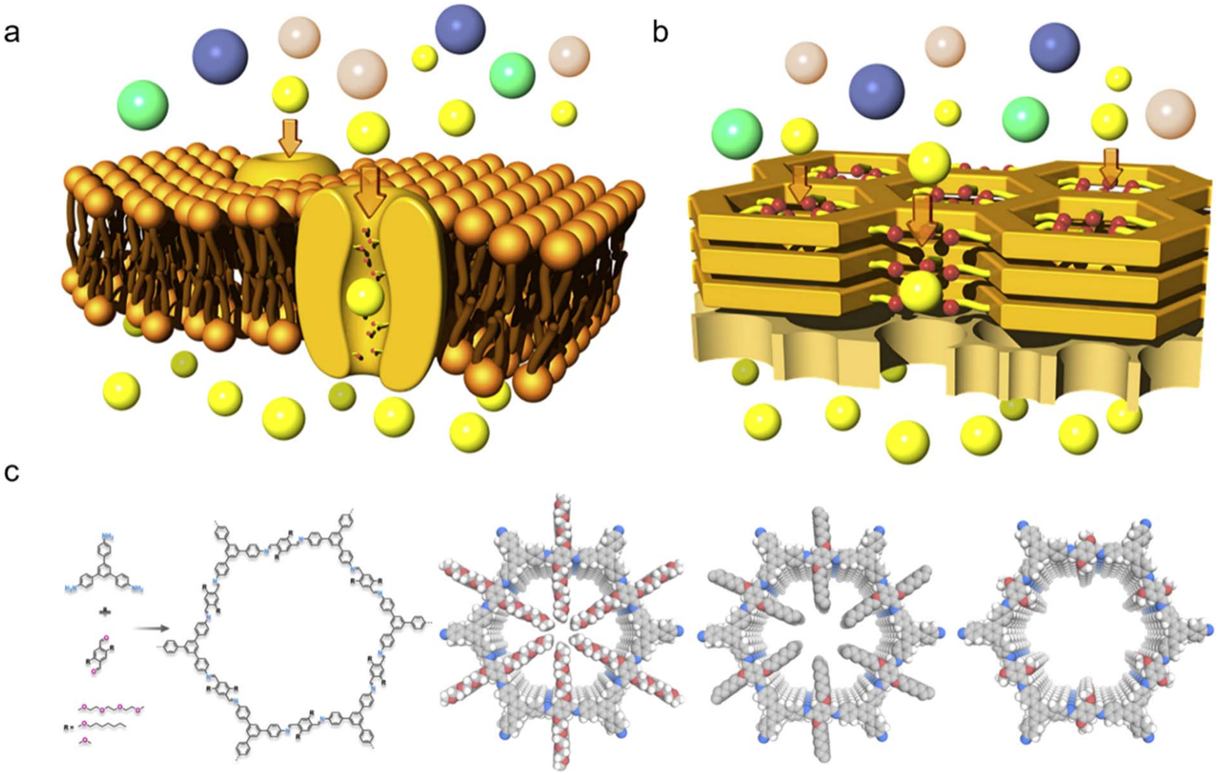

Fig. 8 Biomimetic architecture design of COF membranes. (a) Schematic representation of biological ion channels. (b) Schematic representation of bioinspired artificial ion channels. (c) Schematic illustrations of COF structures derived from TAB reactions with various aldehyde monomers.[88] Copyright 2021, Elsevier.

intense peaks, which signified their tight binding. Conversely, $K^+$–$COO^-$ interactions showed broadened and attenuated peaks corresponding to loose coordination (Fig. 9e). Specifically, approximately 2 $Na^+$ and 0.5 $K^+$ ions occupied the primary coordination shell of carboxylate groups, further confirming the superior binding affinity of $Na^+$ to carboxylate ligands (Fig. 9f). In addition, spatial distribution in the *xy*-plane revealed that both $Na^+$ and $K^+$ ions coordinated with $COO^-$ moieties, accumulating near channel walls with significantly denser $Na^+$ clustering (Fig. 9g). Ion flux was quantified by total ion count, revealing significantly higher $Na^+$ permeation rates and concentrations relative to $K^+$ (Fig. 9h).

Apart from chemical interactions, hydrogen bonding represents a fundamental atomic-scale phenomenon driven by dipole–dipole forces. This interaction occurs when a hydrogen atom, covalently bonded to a highly electronegative element (*e.g.*, O, N, or F), acquires a partial positive charge, enabling electrostatic attraction with another electronegative atom. Leveraging this principle, Sheng *et al.* developed an ultrathin COF membrane ($TpBDMe_2$) featuring abundant hydrogen bonding sites and 1D ordered channels, which showed desirable ion sieving performance (Fig. 10a).[92] The resulting COF membranes exhibited a $K^+/Mg^{2+}$ selectivity of $\approx 765$, alongside a $K^+$ permeation rate of $\approx 0.2$ mol $m^{-2}$ $h^{-1}$. The underlying mechanism for this superior selectivity lies in the hydration shell polarization induced by the high charge density of $Mg^{2+}$, making the hydrogen in water molecules more positively charged and consequently forming hydrogen bonds with COFs to impede $Mg^{2+}$ permeation. This charge effect dictates the hydrogen bonding energy sequence between metal ions and the COF, $K^+ < Na^+ < Li^+ < Mg^{2+}$, consistent with their charge density (Fig. 10b). Concurrently, the average potential energy derived from hydrogen bonding also follows the established sequence: $K^+ < Na^+ < Li^+ < Mg^{2+}$ (Fig. 10c) (Fig. 10c). Furthermore, density functional theory (DFT) calculations show that ion migration resistance, manifested as transmembrane energy barriers, follows the same sequence ($K^+ < Na^+ < Li^+ < Mg^{2+}$). This fundamentally elucidates the origin of the exceptional selectivity (Fig. 10d).

## 3 Guiding principles for COF/MOF membrane design

The dominant mechanisms dictating ion transport and, consequently, separation efficiency in COF/MOF membranes are intrinsically linked to two critical parameters: pore size and the immediate chemical environment. In this context, future design paradigms for high-performance ion-selective COF/MOF membranes must strategically leverage the precise tuning of both pore dimensions and their localized chemical functionalities.

### 3.1 Building block design for COF membranes

COF membranes are porous crystalline structures formed by the periodic covalent linkage of organic building blocks,

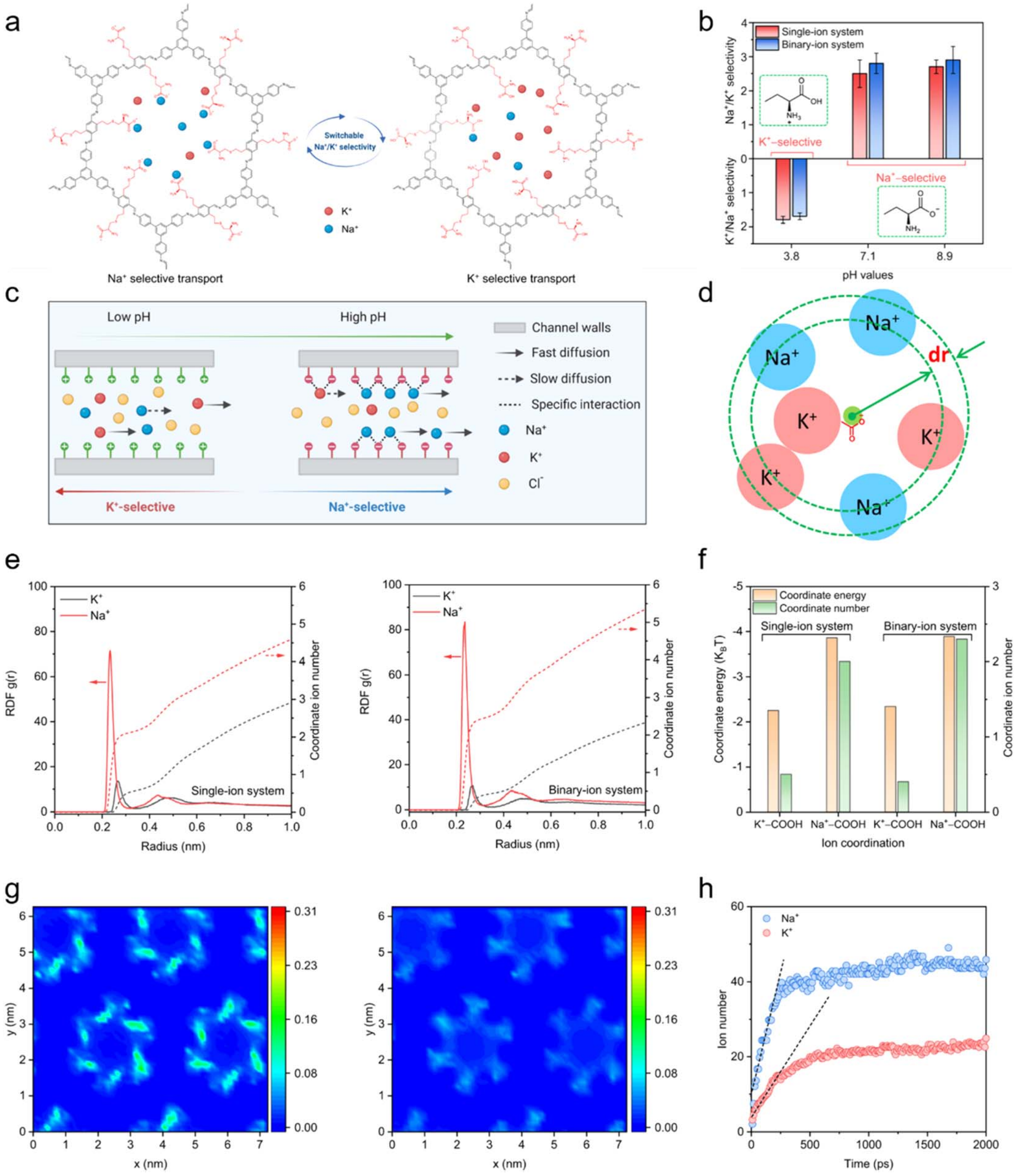

Fig. 9 Engineering pH-responsive COF membranes. (a) Schematic representation of the cysteine-modified COF architecture. (b) Switchable $Na^+/K^+$ selectivity. The inset depicts amine groups' protonation and carboxyl groups' deprotonation, respectively. (c) Schematic of pH-mediated ion transport behavior. (d) Schematic of $Na^+/K^+$ surrounding cysteine. (e) RDF of $Na^+/K^+$ around cysteine. (f) Ionic coordination behaviors around carboxyl groups. (g) Visualization of $Na^+$(left) and $K^+$(right) distributions in mixed-salt solutions. (h) Time-dependent cation concentration profiles.[91] Copyright 2022, Springer.

showcasing excellent long-range order.[93–96] The intrinsic advantages of their definite porosity and programmable chemical microenvironments have established COF membranes as compelling materials for creating intelligent sub-nanometer channels that demonstrate remarkable ion-sieving accuracy.

Advances in topological chemistry, dynamic covalent chemistry, and computational chemistry have illuminated how the symmetry and reactivity of its building blocks affect the structure of a COF membrane. This understanding has advanced the building block design, allowing for the precise, on-demand construction of desired COF structures and functions. A prime example is the strategic utilization of side chain properties, including steric hindrance and electron cloud distribution, to precisely control intrinsic pore size, interlayer stacking mode, topological structure, and the local chemical environment of the COF membrane. Therefore, side chain engineering exemplifies an atomic-scale approach to structural design within the broader context of building block optimization.[97–99]

A key aspect of building block design is the ability to introduce bulky groups, which occupy free volume within the intrinsic channels of COF membranes. This steric hindrance

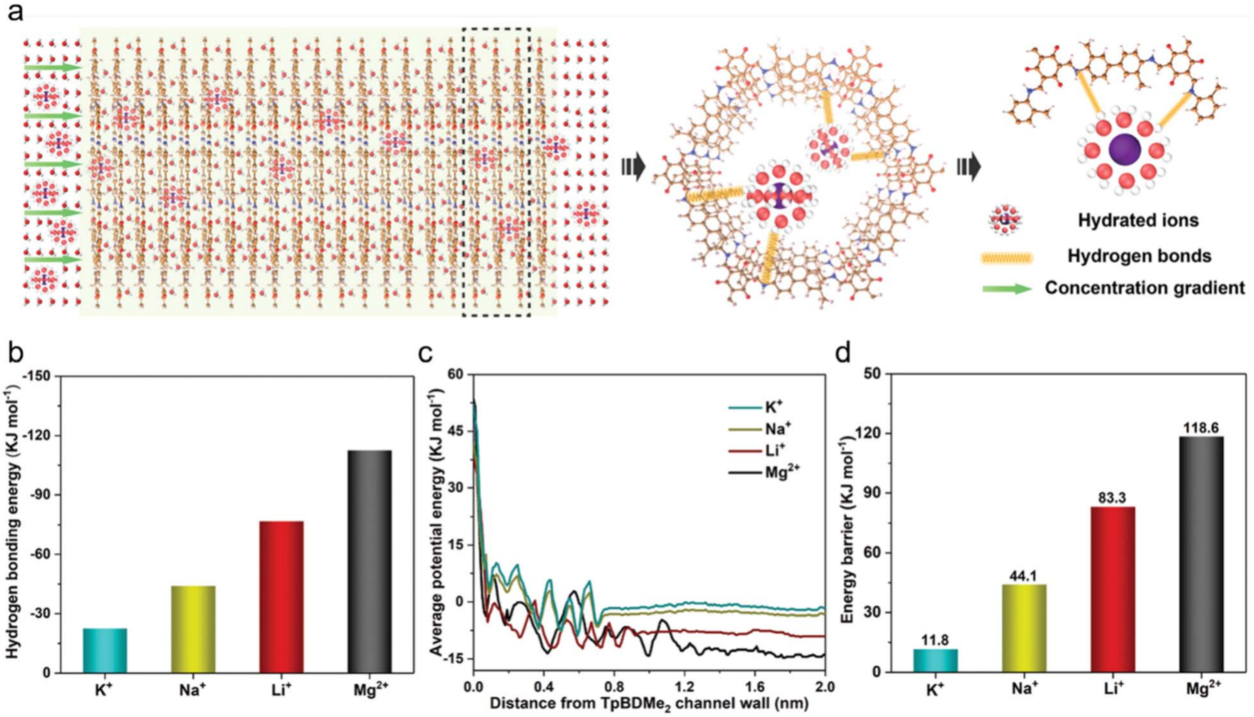

Fig. 10 Hydrogen-bonding-inspired design of COF membranes. (a) Hydrogen-bond-mediated diffusion behaviour. (b) Hydrogen bond energies between ions and COFs. (c) Average potential energy of ions. (d) Energy barriers for ion transport.[92] Copyright 2021, Wiley-VCH.

mechanism provides a useful means to precisely regulate their effective pore size. Illustratively, Liu *et al.* demonstrated the precise regulation of the pore size of a COF membrane—and subsequent removal of small molecular pollutants—by incorporating alkyl chains of varying lengths. Beyond direct engineering of building units, COF pore size can also be indirectly tuned by altering its topology or stacking patterns.[100]

Topology, defined by the specific knot and linker structures, dictates the connection mode and spatial arrangement of building units, thereby offering a means for precise control over the pore structure.[101–103] A notable illustration involves the construction of both single-pore rhombic and dual-pore kagome topologies from identical building blocks (a tetrafunctional $C_2$ knot and a linear $C_2$ linker).[104,105] Expanding on this, Peng *et al.* successfully engineered diverse COF powder architectures by leveraging intermolecular hydrogen bonds. Specifically, in TPE–COF–OH, intramolecular hydrogen bonds induce a *cis* conformation of the imine and olefin bonds, resulting in the characteristic dual-pore (7 Å and 27 Å) kagome topology (Fig. 11a).[106] In contrast, TPE–COF–OMe exhibits a single-pore rhombic topology due to the *trans* conformation of its imine and olefin bonds. The inherent advantages of dual-pore hierarchical networks suggest significant potential for simultaneously boosting membrane selectivity and permeability.[64,107,108] Supporting this, Sun *et al.* created imine-based COFs with distinct topologies by altering the side-chain lengths of dialdehyde monomers (Fig. 11b).[109] Their findings demonstrated that an increase in alkyl chain length in the aldehyde monomers triggers a topological transition in COF membranes, evolving from single-pore structures (0.53 and 0.70 nm) to a dual-pore architecture (0.83 nm). However, hierarchically porous COF materials typically comprise mesopores that are distinctly larger than the hydrated dimensions of metal ions, posing a challenge for constructing ion-selective COF membranes. Side-chain engineering represents a promising strategy to alleviate this issue. For instance, Jiang *et al.* innovated an amphiphilic hierarchically porous COF membrane by precisely regulating the orientation of functional units within separated pores.[110] This strategic structural innovation leverages steric hindrance to achieve a well-defined spatial distribution of hydrophilic and hydrophobic segments. Specifically, the incorporation of long-chain substituents within the hexagonal mesopores reduces the pore size from 26.5 Å to 17.1 Å while concurrently establishing hydrophobic transport pathways. Simultaneously, hydroxyl groups align preferentially within the micropores, facilitating a hydrophilic microenvironment. These hydrophilic microchannels facilitate the preservation of hydration shells around hydrated ions, thereby enabling superior ion transport.[79] This work provides a novel perspective on matching pore geometry and constructing hydrophilic environments. While building block engineering has proven effective for customizing COF powder pore structures through topological design, this approach remains surprisingly underutilized in COF membrane fabrication. This strategy is considered to offer transformative insights for future ion-selective COF membrane advancements.

Interlayer stacking patterns in two-dimensional COFs are dictated by the interplay of monomer steric hindrance and

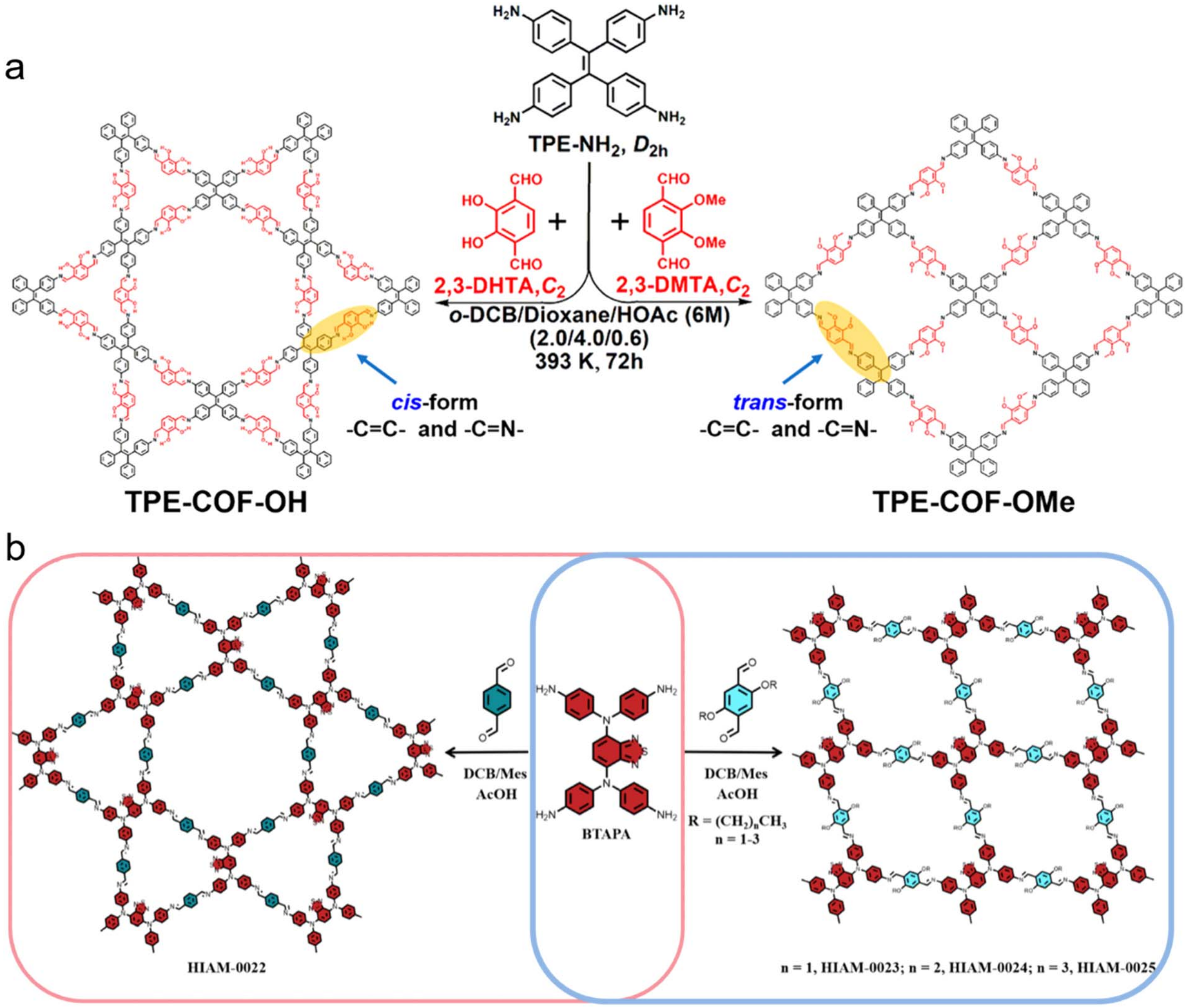

Fig. 11 (a) Topological structure modulation by side-chain chemistry.[106] Copyright 2020, American Chemical Society. (b) Conformational rearrangement through side-chain extension.[109] Copyright 2025, Royal Society of Chemistry.

intermolecular forces.[111,112] Leveraging these interlayer stacking patterns offers a powerful strategy to precisely regulate the pore architecture of COF membranes. Crucially, the eclipsed (AA) stacking of a given COF material results in a stable, larger-pore configuration, while the staggered (AB) stacking corresponds to a metastable state with approximately half the pore size.[113,114] Wu *et al.* exemplified this control in COF powders by strategically introducing isopropyl groups into amine monomers to modulate interlayer stacking *via* steric hindrance. Their findings showed that low isopropyl concentrations favored AA stacking, which provided sufficient interlayer space for minimal isopropyl group rotation. In contrast, higher isopropyl concentrations promoted ABC stacking to achieve optimal crystalline packing energy. This structural control directly translated to porous properties, with AA-stacked COFs exhibiting mesopores and ABC stacking yielding micropores.[115] Moreover, Tian *et al.* presented a ternary building block engineering strategy for high-efficiency hydrogen purification membranes.[116] The results revealed that alkyl chains synergistically occupied free volume and induced an AA-to-AB stacking transition, narrowing pore apertures from 1.4 nm to 0.6 nm. The formation of the AB stacking is attributed to a favorable balance where van der Waals forces effectively compensate for the reduced π–π interactions caused by interlayer offset, resulting in a lower binding free energy. Additionally, steric hindrance from the alkyl chains resulted in an entropy effect, further driving the observed interlayer displacement.

In addition to tailored pore architectures, the structural tunability of COF monomers can also be utilized to impart enhanced antifouling properties to ion-selective membranes. For actual water treatment, the presence of pervasive contaminants leads to the progressive degradation of membrane performance.[117] A widely adopted strategy to enhance membrane antifouling properties involves engineering hydrophilic materials capable of forming a hydration layer at the interface, thereby preventing contaminant adsorption.[118–120] Zwitterionic membranes, characterized by the simultaneous presence of cationic and anionic groups, can couple with water molecules *via* electrostatic interactions and hydrogen bonding, achieving improved antifouling performance.[121] Ji *et al.* exemplified this by pioneering a complementary charge strategy to construct antifouling COF membranes.[122] The results revealed that the complementary charges in zwitterionic systems facilitate the formation of a continuous and dense hydration layer, which effectively suppresses contaminant adsorption through electrostatic repulsion. The resulting zwitterionic COF membranes exhibited significantly lower adsorption capacities for typical anionic contaminants such as bovine serum albumin (BSA) and cationic contaminants such as lysozyme compared to single-ion-type COF membranes, demonstrating their superior antifouling performance.

### 3.2 Post-synthetic modification for COF membranes

Post-synthetic modification (PSM) allows for the precise introduction of organic units or metals into pre-synthesized COFs *via* a range of techniques, including graft modification, dynamic monomer exchange, click reactions, and coordination chelation.[123,124] Among these diverse PSM approaches, graft modification stands out as a versatile strategy, enabling the precise redefinition of COF functionality by anchoring specific motifs onto the framework.

Achieving efficient multi-component differentiation through a single-stage membrane process presents a fundamental challenge. The integration of stimuli-responsive groups into membrane channels offers an effective strategy to address this.[125] For example, Zhao *et al.* successfully grafted photoisomerizable azobenzene groups onto a COF membrane, where subsequent UV irradiation induced *cis–trans* isomerization.[126] This molecular-level change effectively induced a structural transition in the pore architecture (Fig. 12a), allowing for the reversible modulation of the selectivity for differently sized dye molecules and enabling efficient differentiation of multicomponent feed solutions.

Monomer exchange is emerging as a powerful post-synthetic modification strategy for COF membranes, enabling the precise reconstruction of both pore dimensions and chemical microenvironments. This process is thermodynamically driven: if an energy gap exists between COFs formed from a common aldehyde and two distinct amines, the amine of the more stable COF will displace its counterpart in the metastable COF. For instance, imine-based COFs, synthesized *via* dynamic covalent chemistry, readily permit linker exchange to yield a thermodynamically stable framework.[127,128] Specifically, Qian *et al.* demonstrated this by successfully substituting benzidine with *p*-phenylenediamine, precisely tuning the pore sizes of COF powder from initial values of 2.56 nm and 3.91 nm down to 1.61 nm and 3.18 nm, respectively.[129] In addition, Zhang *et al.* reported a novel linker exchange strategy to construct ion-selective COF membranes.[130] This method involved immersing pristine ACOF-1 membranes in a solution of *p*-phenylenediamine, solvent, and acetic acid, leading to the formation of an interlocked COF-LZU1 layer on the ACOF-1 surface. The resulting heterogeneous COF membrane had an average pore size of approximately 0.35 nm, a notable decrease from 0.45 nm in pristine ACOF-1, validating the pore size modulation *via* linker exchange. Notably, the original ACOF-1 membrane demonstrated negligible sodium sulfate rejection, whereas the modified membrane achieved an impressive rejection rate of approximately 97% following 3 hours of linker exchange.

In COF membranes, the polarity of sub-nanometer channels is closely related to both the side-chain functional groups and the chemical bonds within the framework. Specifically, less polar imine bonds result in hydrophobic transport pathways. In contrast, amide linkages, which contain polar oxygen and amino groups, can form intermolecular hydrogen bonds, creating a heightened structural polarity suitable for the transport of polar solvents.[131] Maschita *et al.* validated the conversion of imine-to-imide bonds in COFs *via* alcohol-assisted solvothermal synthesis coupled with monomer exchange. The resulting imide-linked COF powder, featuring strongly polar carbonyl groups, readily engages in hydrogen bonding or dipole–dipole interactions with water molecules, thus confirming that this strategy is effective for tuning channel polarity.[132]

The integration of powerful click chemistry tools, such as thiol–ene click reactions,[133,134] and azide–alkyne cycloaddition,[135] has advanced the design and synthesis of functional COF materials. Capitalizing on this, Jing *et al.* successfully functionalized a COF membrane with various organic units (–COOH, $-NH_2$, or $-SO_3^-$) to achieve gradient channel partitioning (Fig. 12b).[136] The heterogeneous distribution of these units within the nanochannels stems from differential chain flexibility and click reaction kinetics. Specifically, the $-NH_2$ units demonstrated the most favorable chain flexibility and fastest reaction kinetics, resulting in both a high grafting density and a uniform spatial distribution. In addition, the click reaction is catalyzed by copper ions, which not only facilitate the immobilization of the units but also coordinate with their functional groups. This coordination promotes chain entanglement, effectively segmenting the pore channels. This combined effect of pore segmentation and $CO_2$ affinity contributes to the high $H_2/CO_2$ selectivity for amine-functionalized membranes. Furthermore, Meng *et al.* modified COF membranes using cysteamine hydrochloride, precisely tuning the average pore size from 0.38 nm to 0.3 nm, which significantly increased the mono-/multivalent ion selectivity.[45]

### 3.3 Building block design for MOF membranes

In 1990, drawing inspiration from zeolites, Robson *et al.* pioneered the construction of crystalline porous networks *via* metal–oxygen bonds. This seminal work led to the development of a novel class of organic–inorganic hybrid materials, subsequently termed metal–organic frameworks (MOFs).[137,138] MOFs, distinguished by their topological diversity, well-defined porosity, and exceptional surface area, have since become a focal point of extensive research interest.

For isoreticular MOFs, the distance between metal nodes is critically determined by the length of their organic linkers, which function as essential "molecular bridges" between adjacent metal clusters.[139] Deng *et al.* leveraged this by engineering

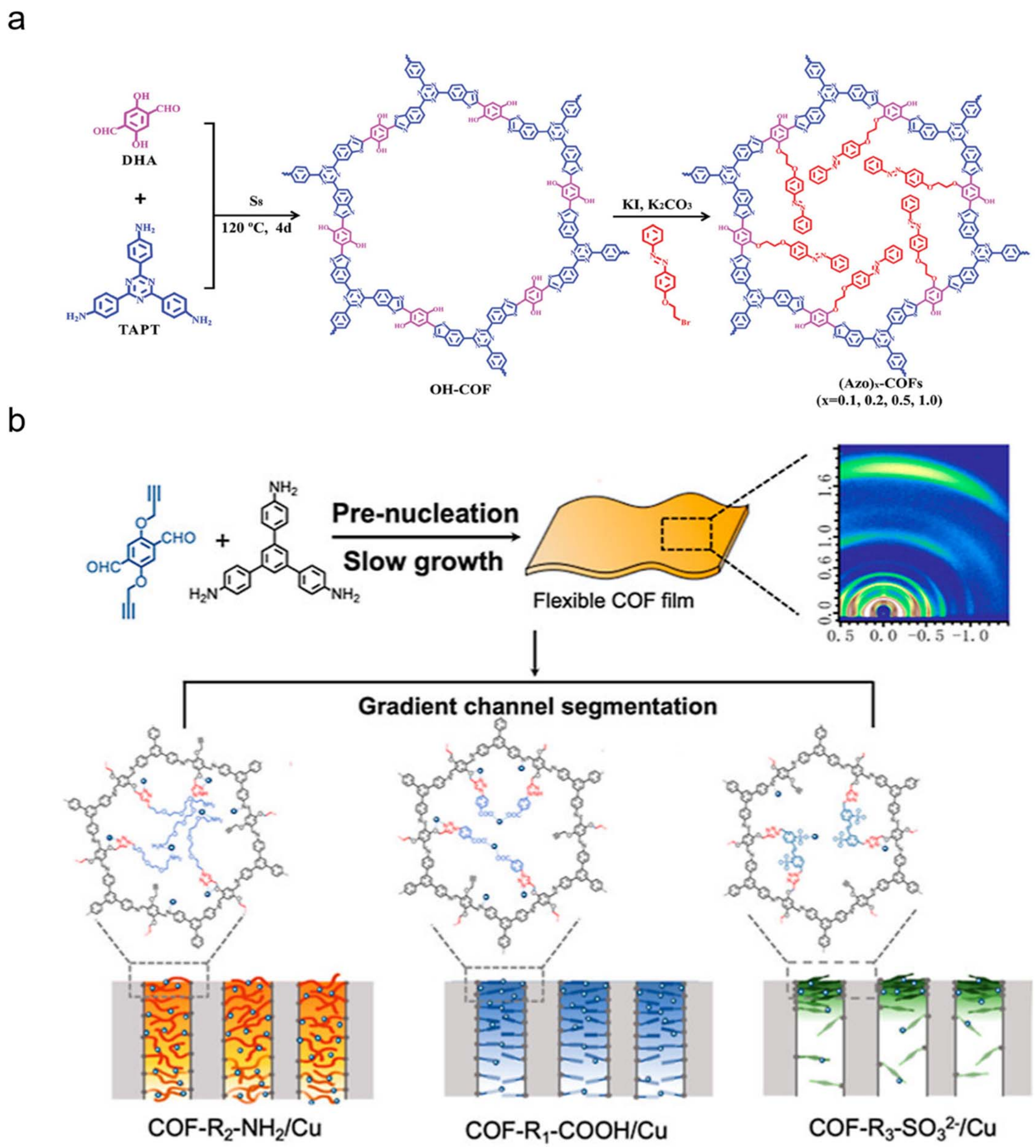

Fig. 12 (a) Incorporating stimuli-responsive units through post-synthetic modification.[126] Copyright 2024, Wiley-VCH. (b) Gradient channel segmentation *via* click reaction.[136] Copyright 2023, American Chemical Society.

organic linker lengths from 7.0 to 50 Å, successfully constructing a series of MOF-74 materials with identical topology yet tunable pore dimensions (Fig. 13a).[140] This yielded MOF materials with impressive pore sizes ranging from 14 to 98 Å. Analogous to COF materials, the non-reactive groups integrated within the periodic porous framework of MOFs significantly affect both their pore architecture and localized chemical microenvironment. For instance, Banerjee *et al.* constructed a series of isoreticular MOF materials by introducing diverse functional groups into organic linkers, where the steric hindrance of these groups effectively led to a decreased pore size (Fig. 13b).[141] The results revealed a general trend of decreasing $CO_2$ uptake capacity with shrinking pore size; however, ZIF-82 and ZIF-78 presented a notable exception, exhibiting enhanced $CO_2$ affinity due to stronger host–guest interactions.

In view of pore size engineering for Zr-MOF membranes, Cong *et al.* strategically adopted three distinct approaches: functional group modification, ligand ratio control, and ligand length adjustment, leading to the successful fabrication of UiO-66, UiO-66-33Br, and MOF-801 membranes for isomer separation.[142] Their precise functional group modification involved partially replacing 1,4-benzenedicarboxylate (BDC) ligands with bulkier 2-bromoterephthalate (BDC-Br) during the secondary growth of UiO-66-33Br selective layers on α-$Al_2O_3$ substrates. Notably, the rational ligand ratio (33 mol% BDCBr) played a key role in effectively narrowing the pore apertures, resulting in superior separation performance for *n*-hexane/2-

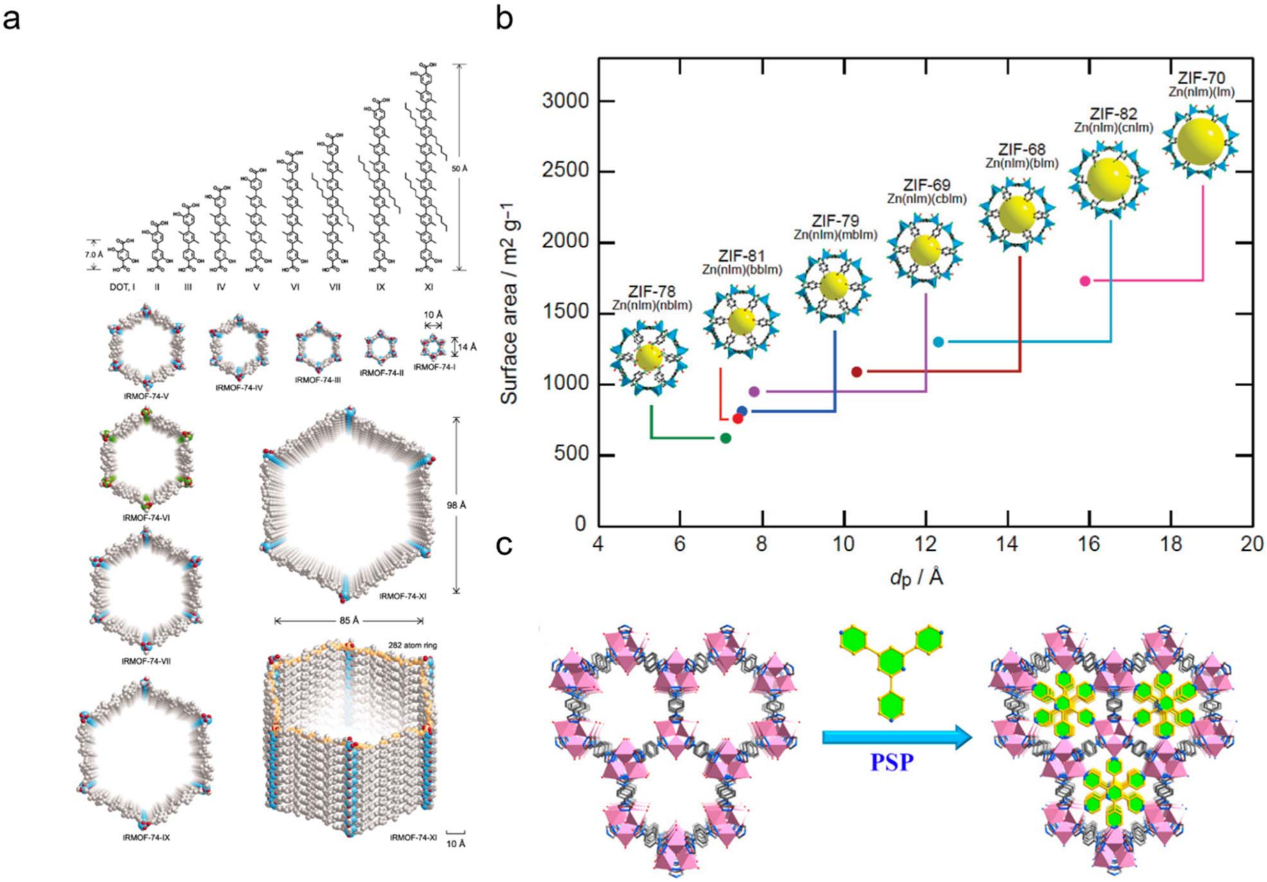

Fig. 13 (a) Engineering MOF architecture *via* design of organic ligands.[140] Copyright 2012, The American Association for the Advancement of Science. (b) Engineering MOF architecture *via* side chains.[141] Copyright 2009, American Chemical Society. (c) Pore space partitioning through axially coordinated organic units.[144] Copyright 2019, American Chemical Society.

methylpentane. Additionally, the application of shorter fumarate ligands during *in situ* solvothermal synthesis facilitated the formation of MOF-801 membranes with highly restricted pores, capable of discriminating *n*-butane from isobutane.

Furthermore, Mo *et al.* engineered functionalized UiO-66 membranes by incorporating organic ligands with precisely tailored surface groups for efficient mono-/multivalent ion separation, achieving a remarkable $K^+/Mg^{2+}$ selectivity of 542.9.[143] The results elucidated the critical correlation between the binding affinity of these surface functionalities with ions and the corresponding transport activation energy. Specifically, the presence of negatively charged –SH and –OH facilitated the attraction of metal ions through strong electrostatic interactions, resulting in favorable (negative) binding energies. In contrast, positively charged $NH_2$ electrostatically repelled cations and thus resulted in unfavorable (positive) binding energies. Notably, the binding affinity trend UiO-66-$(NH_2)_2$ < UiO-66-$(SH)_2$ < UiO-66-$(OH)_2$ aligns with the observed $K^+/Mg^{2+}$ selectivity.

In a notable study, Ye *et al.* immobilized a $C_3$-symmetric organic ligand (Tripp) within the FJU-88 framework, ensuring axial coordination with the metal center (Fig. 13c).[144] The incorporated Tripp ligands facilitated programmed structural segmentation, which not only regulated the topology but also elevated the rigidity of the framework. In addition to structural alterations, Tripp introduced additional adsorption sites, enabling both size sieving and surface functionalization critical for efficient $C_2H_2/CO_2$ separation. The overarching pore space partitioning strategy, therefore, represents a promising avenue for designing ion-selective MOF membranes by precisely engineering the free volume within mesoporous MOFs.

Apart from building block design, the pore architecture of MOFs is largely impacted by their synthetic conditions, including factors such as the metal–linker ratio, solvent system, and reaction kinetics. Wang *et al.* exemplified this by introducing methanol into the MIL-88B synthesis. The coordination of methanol with metal sites led to framework expansion, eventually stabilizing a large-pore structure.[145] Moreover, the ratio between large-pore and narrow-pore phases in MIL-88B was found to be modulated by the methanol concentration. In addition, incorporating either low-dose additives or species featuring non-preferential coordination with metal constitutes a fundamental means for precise MOF architecture design. For instance, as an exceptionally stable MOF, UiO-66 typically features each zirconium cluster coordinating with twelve organic ligands, resulting in a highly ordered framework with remarkable structural integrity. Cai *et al.* presented an innovative "ligand-deficient" strategy to create mesoporous UiO-66.[146] This involved introducing monocarboxylic acid into the synthesis, where the steric hindrance of its alkyl chains regulated the coordination environment by impeding the complete incorporation of organic linkers. In parallel, monocarboxylic acids form coordination complexes with metals; however, these interactions are preferentially replaced by organic ligands due to the significantly lower $pK_a$ of the latter. Moreover, the insufficient ligand in this work suggested incomplete substitution, resulting in defects in the network. Their findings clearly demonstrate a positive correlation between both the concentration of carboxylic acid and the length of the alkyl chain, and the resulting pore size.

The unique ability of flexible MOF materials to undergo reversible structural rearrangement in response to external stimuli presents an effective avenue for controlled separation. Polyukhov *et al.* demonstrated this principle by developing a temperature-modulated pore regulation strategy based on the "gate-opening effect".[147] A clear relationship between temperature and molecular permeation was established: *p*-xylene permeated at low temperatures, *m*-xylene at moderate temperatures, and *o*-xylene required a significant temperature increase to diffuse through the pores. In a related innovative application, Mukherjee *et al.* engineered IITKGP-39, a flexible twofold interpenetrated 3D MOF, to address the challenging separations involved in ethylene purification and acetylene/carbon dioxide separation.[148] This MOF exhibits three distinct structural phases: as-synthesized (α-phase), activated (β-phase), and gas-adsorbed/gate-opened (γ-phase) forms. The mechanism of action is rooted in a guest-triggered structural change: upon activation, the release of guest molecules causes the internal angle of the rhombic pore to contract. However, the selective adsorption of certain gases expands this angle to 83°, effectively opening the gate for molecular access. The selectivity hinges on the strength of the guest–framework interaction; $C_2H_6$ and $C_2H_2$ exhibit sufficiently strong binding to induce this crucial phase transition, whereas the weaker binding of $C_2H_4$ and $CO_2$ is insufficient to initiate the structural change, thereby enabling the highly selective uptake of the former two gases.

Leveraging the inherent flexibility of MOFs to selectively discriminate between chemically similar species represents a significant opportunity for the rational design of next-generation ion-selective membranes. For instance, Ying *et al.* developed a sophisticated strategy by exploiting the "gate-opening effect" in flexible MOFs to create pressure-responsive membranes for highly selective $CO_2$ separation.[149] It was demonstrated that pressure-induced structural transformations are the result of a gliding motion of phenyl rings within the 2D layers of the framework. Specifically, when the gas pressure surpasses a critical threshold, the framework undergoes adsorption, and the resulting intermolecular interactions drive a reversible architectural evolution. This structural reconfiguration leads to pore dilation, which critically allows for the simultaneous enhancement of both permeability and selectivity, thus overcoming the traditional trade-off limitations in membrane technology.

### 3.4 Post-synthetic modification for MOF membranes

Direct immobilization of specific motifs on MOF building blocks can hinder their crystallization. Therefore, post-synthetic modification (PSM) strategies have been adopted to introduce functional groups into the reticular framework, allowing for precise regulation of the pore architecture and chemical microenvironment. Given that MOF formation is a chemical reaction controlled by both thermodynamic and kinetic factors, the one-step synthesis of mesoporous MOFs frequently encounters challenges such as interpenetrated structures and pore collapse.

Ligand exchange offers a powerful approach to circumventing the limitations of conventional MOF synthesis, particularly for creating mesoporous structures. A notable example is the solvent-assisted ligand exchange method developed by Karagiaridi *et al.*, which enables the extension of MOF organic pillars and the enlargement of pore dimensions.[150] Their findings indicate that ligands with higher affinity for zinc are preferentially incorporated into the framework, highlighting that the Zn–ligand bond strength, which correlates with the $pK_a$ of the conjugate acid, is crucial for the exchange process.

Another effective method leverages the metal ions or metal–oxo clusters within the MOF network. These sites, possessing vacant orbitals, can act as reactive sites for coordinating with organic building units. This principle was exploited by Han *et al.*, who used coordination chemistry to introduce chirality into MOFs by anchoring L-lactic acid onto the open magnesium sites of a pre-activated framework.[151] The partial occupation of channels by these chiral molecules resulted in a reduced pore volume, as confirmed by a decrease in the specific surface area. The newly introduced carboxyl and hydroxyl groups also provided additional coordination sites for metal ions. In a similar vein, Wang *et al.* modified Mg-MOF-74 membranes with ethylenediamine, increasing the $H_2/CO_2$ separation selectivity from 10.5 to 28.[152] In this case, one amino group of the ethylenediamine coordinates with an active metal site on MOF-74, while the other remains exposed within the pore channels to regulate gas molecule transport. The enhanced selectivity is attributed to two main factors: stronger interactions between the amino group and $CO_2$, which reduce $CO_2$ permeability, and the smaller pore size, which imposes more stringent kinetic restrictions on the larger $CO_2$ (3.3 Å) than on $H_2$ (2.9 Å).

## 4 Fabrication approach for the COF/MOF membrane (COFM/MOFM)

The synthesis of COF membranes is a complex process governed by a delicate balance between kinetic and thermodynamic factors, which results in strict reaction conditions and slow crystallization rates. Existing synthetic methods—*in situ* growth, interface-assisted synthesis, and layer-by-layer assembly—have been refined with techniques like substrate modification, the addition of co-solvents and surfactants, and the use of catalysts to achieve high-quality thin films.[153–157] On the other hand, the traditional approach to MOF membrane synthesis involves immersing substrates directly into precursor solutions, where organic linkers and metal ions undergo sequential nucleation, crystallization, and growth. This method is often challenged by the competition between homogeneous nucleation in the solution and heterogeneous nucleation on the substrate, frequently leading to defective and discontinuous membranes.[158] To address this, new strategies such as substrate modification, the use of multi-metallic sources, and seed-assistance have been developed to specifically boost heterogeneous nucleation.

### 4.1 *In situ* growth for COFM synthesis

*In situ* growth involves initially grafting one monomer onto a pre-functionalized substrate, followed by submerging the substrate in a solution containing a second monomer, where the active COF layer is formed through hydro-/solvothermal synthesis. The porous substrate is crucial, as it serves as a reactive zone with heterogeneous nucleation sites that guide the uniform growth of the COF layer.[159–162]

While the thermal stability of inorganic carriers meets the requirements for the elevated temperatures for *in situ* growth, achieving sufficient interfacial compatibility between the inorganic support and the active COF layer remains a key challenge. To address this, the surfaces of inorganic substrates are routinely modified with reagents like polyaniline (PANI), 3-aminopropyltriethoxysilane (APTES), and 3-aminopropyltrimethoxysilane (APTMS) to enhance interfacial adhesion and promote uniform film growth. Wang *et al.* exemplified this by decorating an $Al_2O_3$ substrate with APTES to provide heterogeneous nucleation sites for the growth of COF-300 membranes.[163] The method involved grafting APTES onto the $Al_2O_3$ surface to anchor terephthalaldehyde (TPA) molecules, achieving uniform nucleation and growth of the COF-300 active layer. The resulting membrane exhibited impressive operational stability over a continuous 90-hour cross-flow test. In parallel, Liu *et al.* employed surface-initiated polymerization to successfully grow TpPa-$SO_3H$ layers on an amino-functionalized oxide surface (Fig. 14a).[164] The superior polymerization kinetics in this method are attributed to the pre-assembled APTMS monolayer, which provides specific amine binding sites that direct the COF growth upon immersion in the precursor solution.

Due to their high cost and lack of flexibility, the use of inorganic substrates poses a significant challenge for large-scale industrial applications. This has resulted in growing interest in the utilization of porous polymeric substrates such as polyacrylonitrile (PAN), nylon, and polysulfone (PSF).[165] These materials are advantageous because their intrinsic functional groups (*e.g.*, carboxyl or amino groups) can promote COF nucleation and growth under mild or ambient conditions. In addition to using pristine polymer surfaces, various modification strategies have been developed to introduce additional reactive sites.[166] Examples include using alkaline hydrolysis to convert nitrile groups into carboxyl groups or applying polydopamine deposition to create surfaces rich in amino groups.[167,168]

Shen *et al.* demonstrated a robust method for fabricating high-performance membranes by using polydopamine (PDA)-modified polyacrylonitrile (PAN) surfaces.[167] The PDA layer effectively anchors building blocks, thereby facilitating the uniform nucleation and growth of a sulfonic COF (SCOF). The resulting SCOF membrane demonstrated an exceptional water permeance of 134.6 L $m^{-2}$ $h^{-1}$ $bar^{-1}$ while maintaining >99.0% rejection of various organic molecules such as Eriochrome black T and Congo red. In contrast, an unmodified PAN substrate failed to provide the necessary heterogeneous nucleation sites, a deficiency attributed to insufficient interfacial compatibility between the SCOF microcrystals and the substrate. This led to the formation of a defective active layer consisting of loosely packed, fibrous SCOF assemblies. The poor interfacial adhesion was evident from the membrane's lightening after ultrasonication, and its compromised structure resulted in negligible separation performance.

Wu *et al.* developed a sophisticated functionalization strategy for PAN substrates, which involved incorporating additional amine groups *via* APTES modification. This step successfully created a high density of active nucleation sites for the subsequent 3D COF growth (Fig. 14b).[169] The resulting membrane demonstrated an exceptional $Li^+$ permeation rate of 0.123 mol $m^{-2}$ $h^{-1}$, a superior $Li^+/Mg^{2+}$ selectivity of 36, and outstanding long-term operational stability. This work highlighted that selective $Li^+/Mg^{2+}$ transport is collectively governed by size sieving, ion affinity interactions, and electrostatic interactions.

### 4.2 Layer-by-layer assembly for COFM synthesis

Layer-by-layer assembly enables the construction of thin films through the sequential deposition of 2D COF nanosheets (CONs). CONs are typically fabricated using two distinct pathways. The first is a top–down strategy,[170,171] in which bulk COFs are exfoliated using methods such as solvent sonication, mechanical stripping, or chemical intercalation. The second is a bottom–up approach,[172,173] which enables direct nanosheet synthesis through self-exfoliation or interfacial growth techniques.

Zhu *et al.* developed defect-free COF-based ion-selective membranes (denoted as DhaTGCl/TpPa-$SO_3H$) based on electrostatic interactions (Fig. 15a).[174] The CONs were fabricated in a stable colloidal dispersion using an oil–water–oil triphasic system before being deposited onto substrates *via* vacuum-assisted filtration. The oppositely charged nanosheets created an interlocked conformation that stabilized the interlayer architecture, leading to marked pore size reduction. This structural change resulted in a superior salt rejection rate of 99.99% and exceptional long-term stability over 156 hours of continuous operation. Furthermore, the high aspect ratio (>10 000) of the interlocked CONs significantly shortened the water transport pathway, thereby giving rise to a high permeance of 132.66 kg $m^{-2}$ $h^{-1}$.

Zheng *et al.* engineered hetero-charged COF membranes from oppositely charged CONs with different pore sizes, achieving exceptional rejection efficiency for multivalent ions such as $Ni^{2+}$, $Cd^{2+}$, $Cr^{2+}$, $CrO_4^{2-}$, and $SeO_3^{2-}$ (Fig. 15b).[175] This superior performance is a result of the synergy between steric

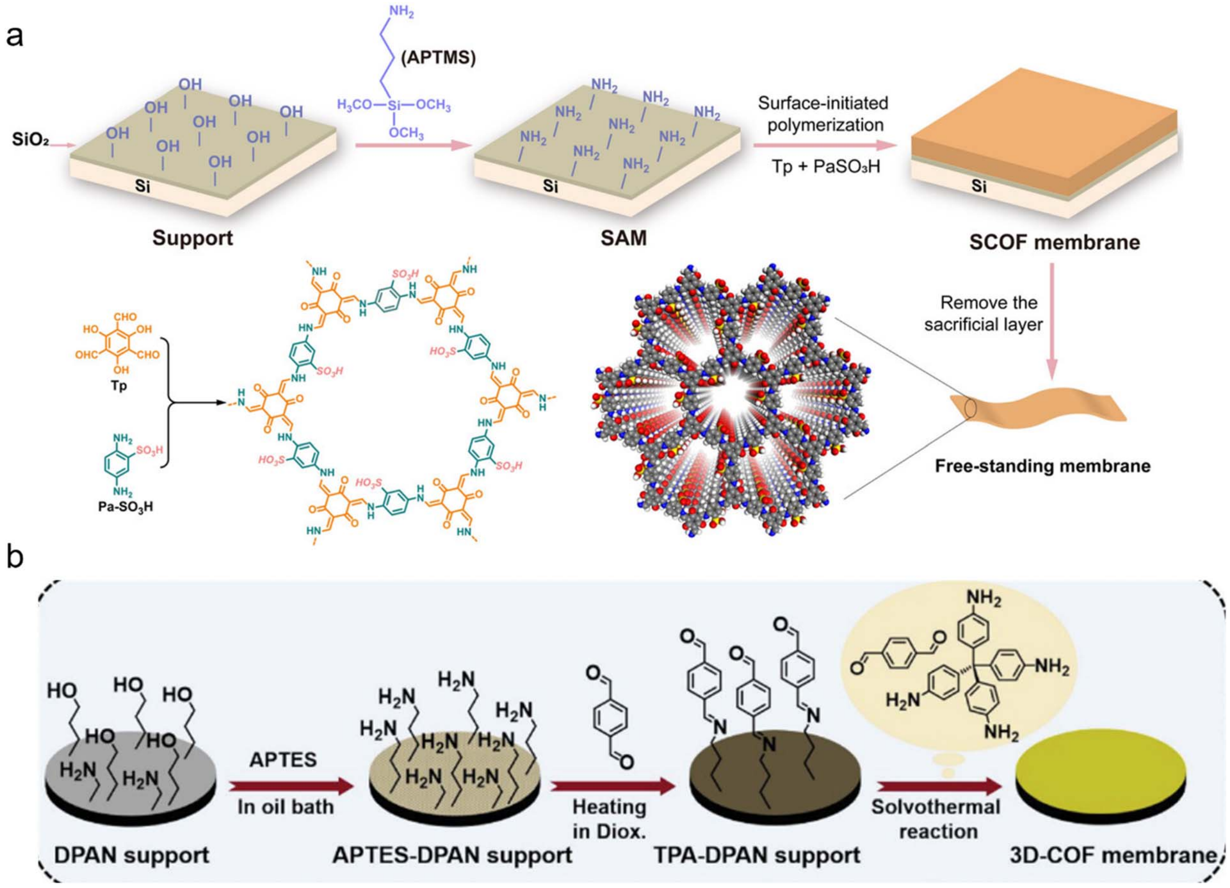

Fig. 14 (a) APTES monolayer initiated COF growth on silicon wafers.[164] Copyright 2021, Wiley-VCH. (b) Aldehyde-functionalized PAN substrates.[169] Copyright 2025, Wiley-VCH.

hindrance and Donnan exclusion, stemming from the intrinsic pore size mismatch and the hetero-charged structure. The LBL assembly method proved highly advantageous, enabling precise tuning of membrane properties (*e.g.*, thickness, hydrophilicity, pore size, and zeta potential) by facile alteration of the ratio of the two nanosheet dispersions. The resulting membrane also demonstrated remarkable stability due to favorable π–π stacking interactions, maintaining its performance during 7 days of continuous operation for heavy metal removal. In parallel, Wang *et al.* successfully constructed staggered-stacking COF membranes from oppositely charged CONs, leveraging electrostatic interactions to synergistically enhance both mechanical integrity and separation efficiency (Fig. 15c).[176] The resulting staggered-stacking COF membranes showed a two-fold increase in mechanical performance compared to single-component COF membranes. Additionally, the staggered-stacking COFM achieved a monovalent salt ion rejection rate of 77.9%, a substantial increment over the 49.2% rejection rate observed in single-component membranes.

### 4.3 Interfacial polymerization for COFM synthesis

Interfacial polymerization (IP) has emerged as a burgeoning platform for the on-demand design of ultrathin COF membranes, as it exploits fundamental thermodynamic and kinetic principles such as dissolution, partitioning, equilibrium, and phase separation.[177–180] In this approach, the substantial polarity difference between these phases confines the condensation reaction to the interfacial region, which is crucial for yielding ultrathin films with precisely controlled thickness. The judicious selection of diverse interfaces has been shown to effectively manipulate the nucleation and crystallization processes, thus enabling the construction of COF membranes with well-defined architectures.[181–183]

Surfactants are known to reduce the interfacial tension and enhance the diffusion of monomers, thereby accelerating interfacial polymerization reactions. Capitalizing on this principle, Du *et al.* created a minute-scale interfacial polymerization process by using sodium dodecyl sulfate (SDS) as a molecular bridge at the water–dichloromethane interface (Fig. 16a).[184] This molecular bridge facilitated the diffusion of tris(4-aminophenyl)amine (TAPA) by creating strong electrostatic interactions between protonated TAPA and the negatively charged head of the SDS molecule. A key benefit of this method is that the SDS addition not only prevented powder formation but also facilitated the formation of a dense film with a sharper pore size distribution.

In addition, solvents play a dual role in interfacial polymerization: as a key determinant of the reaction and as a medium

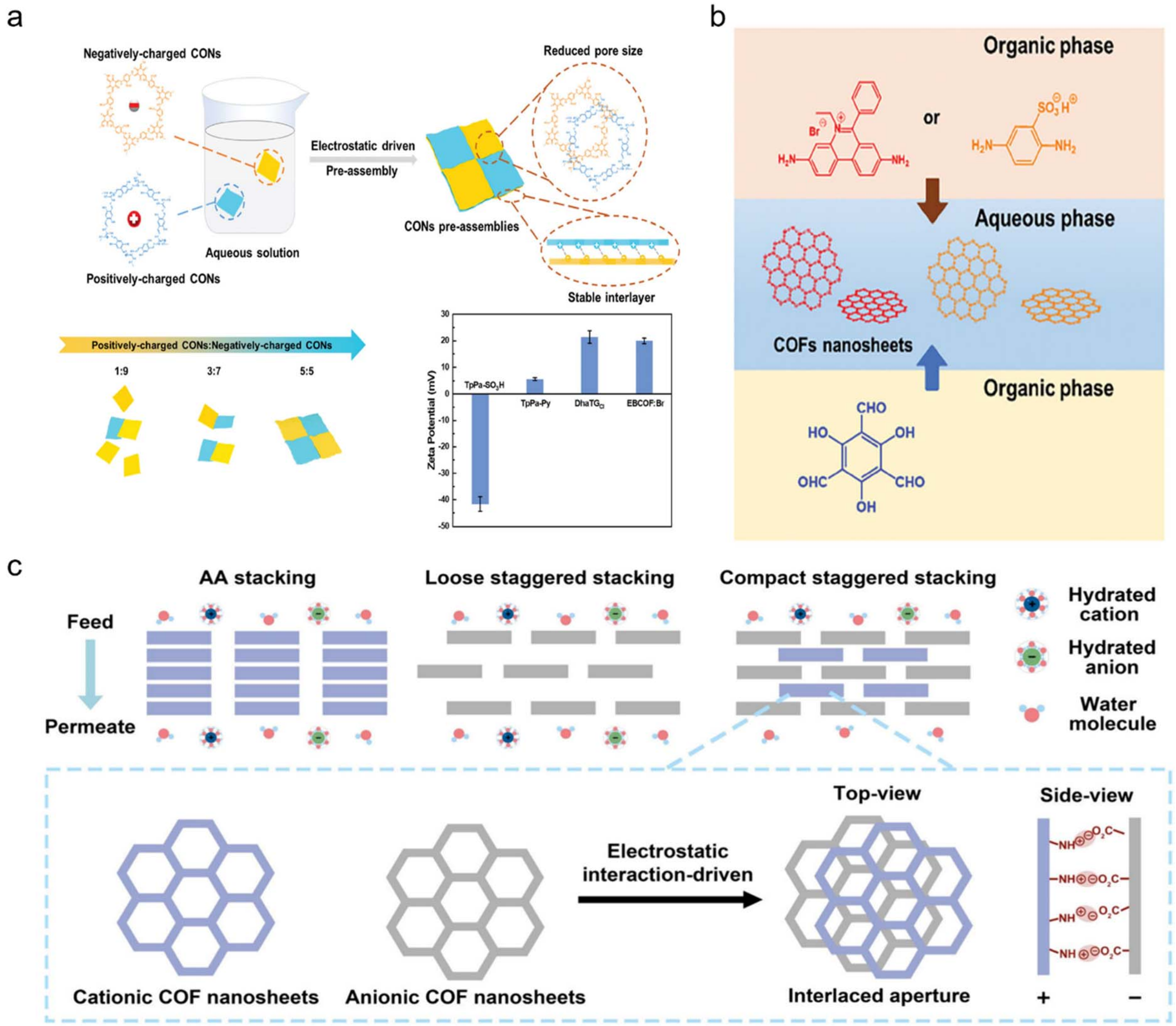

Fig. 15 (a) Interlocked CONs formed *via* electrostatic interaction.[174] Copyright 2024, Wiley-VCH. (b) Engineering membrane architecture with pore size mismatch and heterogeneous charges.[175] Copyright 2024, Wiley-VCH. (c) Electrostatic-mediated stacking configurations of CONs.[176] Copyright 2024, American Chemical Society.

for green synthesis of membranes.[185] In the context of sustainable fabrication, green solvents—including ionic liquids, aqueous two-phase systems (ATPSs), and deep eutectic solvents—are particularly effective.[186] Expanding on this, Wang *et al.* utilized an ATPS composed of polyethylene glycol (PEG) and dextran (Dex) to create separate aqueous phases for dissolving aldehyde and amine monomers (Fig. 16b).[187] This system allowed for the precise tuning of interfacial tension by modulating the polymer ratio. It was found that a higher interfacial tension (0.1–1.0 mN $m^{-1}$) promoted the formation of dense and continuous membranes, whereas a lower tension (0.001–0.1 mN $m^{-1}$) led to porous and fragile architectures. The resulting optimized membranes exhibited outstanding performance, achieving NaCl rejections of 93.0–93.6% and a water permeance of 1.7–3.7 L $m^{-2}$ $h^{-1}$ $bar^{-1}$, outperforming conventional COF membranes.

Freestanding COF nanofilms often suffer from inferior mechanical properties and are difficult to handle, with subsequent transfer to a porous substrate leading to weak interfacial adhesion. To address these challenges, thin-film composite membranes can be fabricated through *in situ* reactions by placing the substrate directly at the interface.[183] Wang *et al.* successfully demonstrated this by developing an *in situ* interfacial polymerization technique that employs electrochemical deprotonation and electric field-induced migration to grow a COF active layer onto a PAN substrate (Fig. 16c).[188] A key finding was the emergence of a self-healing mechanism during the electrochemical interfacial polymerization, which ensured a continuous and defect-free membrane architecture. This effect is driven by preferential polymerization that occurs at defect sites, where the localized current density is highest. Consequently, the resulting COF membrane showed outstanding desalination performance, achieving a water permeance of 92 kg $m^{-2}$ $h^{-1}$ and an outstanding salt rejection of 99.96%, which is superior to the performance of most reported ion-selective COF membranes.

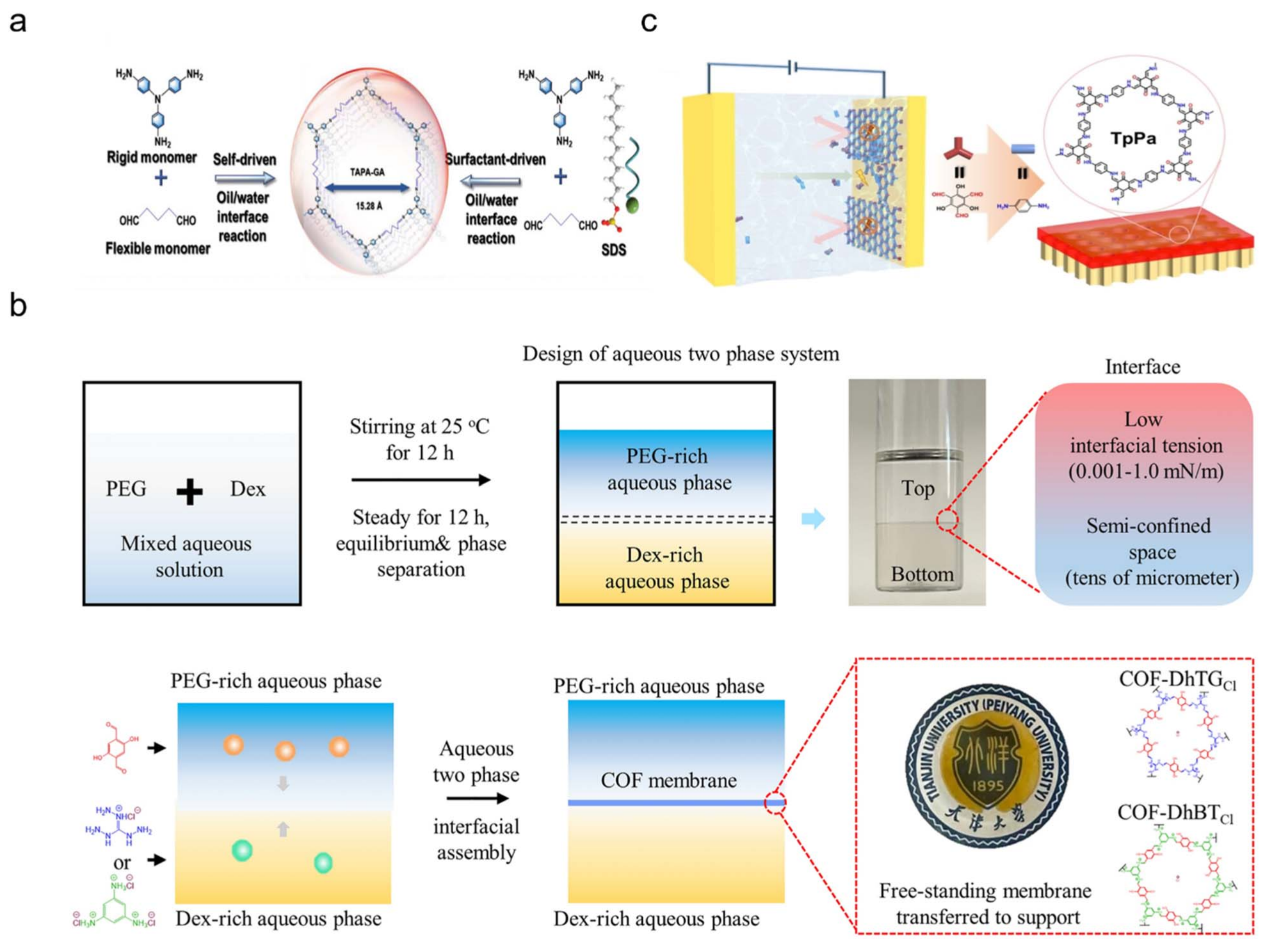

Fig. 16 (a) Surfactant-assisted interface polymerization.[184] Copyright 2023, Wiley-VCH. (b) Schematic of aqueous two-phase interface polymerization.[187] Copyright 2023, Wiley-VCH. (c) Electrochemical interface polymerization for ultrathin COF membrane fabrication.[188] Copyright 2022, Springer.

### 4.4 *In situ* growth for MOFM synthesis

Paralleling the solvothermal/hydrothermal synthesis of bulk MOFs, the *in situ* growth of MOF membranes (MOFMs) relies on elevated temperatures to enable the formation of active layers from precursor solutions on various substrates. A representative example is the work reported by Liu and co-workers, who fabricated an ultrathin MOF-5 active layer on an $\alpha$-$Al_2O_3$ substrate.[189] A combined pretreatment using 1,4-benzenedicarboxylic acid (BDC) and anhydrous zinc nitrate was found to be instrumental in achieving the growth of a continuous MOF-5 membrane. The resulting membranes exhibited gas permeance reaching approximately 65% of that of the pristine substrate, suggesting the formation of a MOF active layer.

A critical challenge for *in situ* grown MOFMs lies in the lack of favorable interactions between porous substrates and metal ions, which diminishes heterogeneous nucleation sites yet promotes undesirable homogeneous nucleation in the bulk solution.[190] A promising strategy to address this is the exploitation of a bimetallic source methodology to create heterogeneous nucleation sites, which in turn optimizes interfacial compatibility between the substrate and the nascent MOF microcrystals. For instance, the incorporation of zirconium ions directly onto a substrate has been shown to successfully facilitate interfacial heterogeneous nucleation, allowing the formation of a continuous UiO-66 membrane. Liu *et al.* exemplified this by engineering a UiO-66 active layer *via in situ* growth on pre-structured yttria-stabilized zirconia (YSZ) hollow fibers, enabling organic dehydration through pervaporation.[191] Their findings revealed a unique growth mechanism where metal ions and organic ligands first formed gel particles in the precursor solution. These particles subsequently migrated to and accumulated on the YSZ hollow fiber surface *via* Brownian motion, a process driven by the coordination between zirconium atoms on the substrate and ligands within the gel particles. This persistent deposition of gel particles led to continuous crystal growth, eventually forming a highly interconnected MOF active layer. Moreover, Guo *et al.* reported a method where a heat-treated copper mesh was immersed in a solution of copper nitrate and trimesic acid.[192] In this process, both the copper oxide on the substrate surface and the copper ions in solution acted as metal sources, facilitating nucleation and growth to produce a continuous MOF layer.

Surface functionalization with metal-ion-anchoring reagents is a beneficial approach to promote heterogeneous nucleation kinetics. A notable approach is inspired by mussel bioadhesives, where dopamine undergoes oxidative self-polymerization under oxygenated, humid, and weakly alkaline conditions. This process yields polydopamine (PDA) oligomers that assemble into a layer with remarkable adhesive properties due to synergistic covalent and non-covalent interactions.[193] Xie *et al.* exemplified this by engineering a PDA-modified regenerated cellulose membrane *via* interfacial self-polymerization. The PDA interlayer functioned as a secondary functional platform, anchoring metal ions to accelerate the heterogeneous nucleation of ZIF-8, which facilitated the *in situ* self-assembly of a uniform and continuous MOF layer that exhibited excellent oil/water separation performance.[194]

A parallel approach was demonstrated by Huang *et al.*, who engineered PDA-modified steel meshes. Here, synergistic covalent and non-covalent interactions with zinc ions promoted the nucleation and growth of defect-free ZIF-8 membranes.[195] In a contrasting and innovative strategy, the same group utilized APTES-modified porous ceramics for ZIF membrane fabrication.[196] The ZIF-22 layer grown on the APTES-modified ceramics was confirmed by a continuous, dense, and defect-free layer (~40 μm thickness), which exhibited superior hydrogen selectivity and thermal stability. This structural integrity stems from the coordination between the 3-aminopropylsilane groups on APTES and zinc ions, which directly facilitates the nucleation and subsequent epitaxial growth of the MOF membranes. In contrast, pristine ceramic substrates yielded discontinuous ZIF-22 deposits characterized by isolated crystalline islands and discrete crystals.

### 4.5 Secondary growth for MOFM synthesis

The secondary growth approach is a powerful seed-assisted strategy for the thin-film fabrication of MOF membranes. This process involves the pre-deposition of crystal seeds on a substrate, followed by immersion in a precursor solution under solvothermal or hydrothermal conditions. Neelakanda *et al.* innovatively combined this technique with a bimetallic-source strategy to create ultrathin ZIF-8 membranes with superior intercrystalline cohesion.[197] Specifically, a ZnO layer was deposited onto a porous polyacrylonitrile (PAN) substrate *via* magnetron sputtering. Upon immersion in a ligand solution, this ZnO layer functioned as a second metal source and formed a seed layer. The seed layer proved critical for two functions: it facilitated the heterogeneous nucleation of ZIF-8 at the interface and simultaneously enhanced the interfacial adhesion between the formed MOF layer and the underlying substrate.

In parallel, Zhai *et al.* developed a bimetallic-source secondary growth strategy in which both the alumina substrate and aluminum ions from the precursor solution serve as synergistic metal sources to create a crucial seed layer (Fig. 17a).[198] The resulting membrane showed exceptional separation performance and structural integrity for pervaporation alcohol dehydration and dye nanofiltration, outperforming MOF-303 membranes prepared using alternative methods. This success highlights a key distinction from MOF membranes fabricated *via* one-step hydrothermal growth, which exhibited random crystal orientation, intercrystalline defects, and weak adhesion.

Apart from using secondary metal sources for seed deposition, another strategy involves first synthesizing precursor suspensions of MOF nanoparticles or nanosheets and then immersing a substrate in them to form a seed layer. Yuan *et al.* successfully utilized this method, depositing ZIF-300 seeds on an $\alpha$-$Al_2O_3$ substrate.[199] These seeded substrates were then immersed in a MOF precursor solution under solvothermal conditions to fabricate a ZIF-300 membrane. The resulting active layer, approximately 10 μm thick, demonstrated exceptional long-term stability and efficiency for heavy metal ion removal in crossflow filtration mode.

In addition, spin-coating and blade-coating represent well-established strategies for seed layer deposition.[200] For instance, Zhang *et al.* successfully spin-coated a dispersion of ZIF-8/GO nanosheets twice on alumina supports, creating a uniform seed layer that served as an epitaxial template for MOF membrane growth.[67] The resulting membrane exhibited exceptional alkali metal ion separation efficiency, driven by synergistic dehydration effects and steric hindrance mechanisms. A particularly innovative method was introduced by Wu *et al.*, who employed a sacrificial polymer binder for blade-coating zirconia seeds (Fig. 17b).[201] The polymer gradually dissolved during solvothermal treatment, creating templated voids that facilitated MOF nucleation and growth. Their findings showed that the polymer played a dual regulatory role: it enhanced the interfacial compatibility between the seeds and the substrate and modulated the formation of UiO-66, enabling the high-quality construction of the MOF layer. Current–voltage (*I*–*V*) measurements further demonstrated that the MOF membrane exhibited hydration-controlled differential ion transport behavior.

### 4.6 Contra-diffusion assisted growth for MOFM synthesis

The counter-diffusion assisted growth approach is a distinct method from *in situ* synthesis, utilizing a substrate to spatially separate organic ligand and metal ion solutions.[202,203] This strategy promotes crystal nucleation and growth exclusively within and on the porous scaffold, allowing for the elaborate architectural engineering of composite membranes. Counter-diffusion synthesis is governed by coexisting reaction and diffusion dynamics, with both parameters having a profound impact on the final structure. As a prime example of modulating the diffusion rate to regulate the reaction zone, Shamsaei *et al.* combined counter-diffusion synthesis with vapor-phase modification to develop an innovative fabrication method for high-quality ZIF-8 composite membranes (Fig. 18a).[204] The modified substrate, with its reduced pore size and freshly introduced amine groups, effectively suppressed the migration of $Zn^{2+}$ ions while enriching them at the substrate interface. This precisely controlled reaction zone enabled the fabrication of continuous, defect-free ultrathin MOF membranes with outstanding

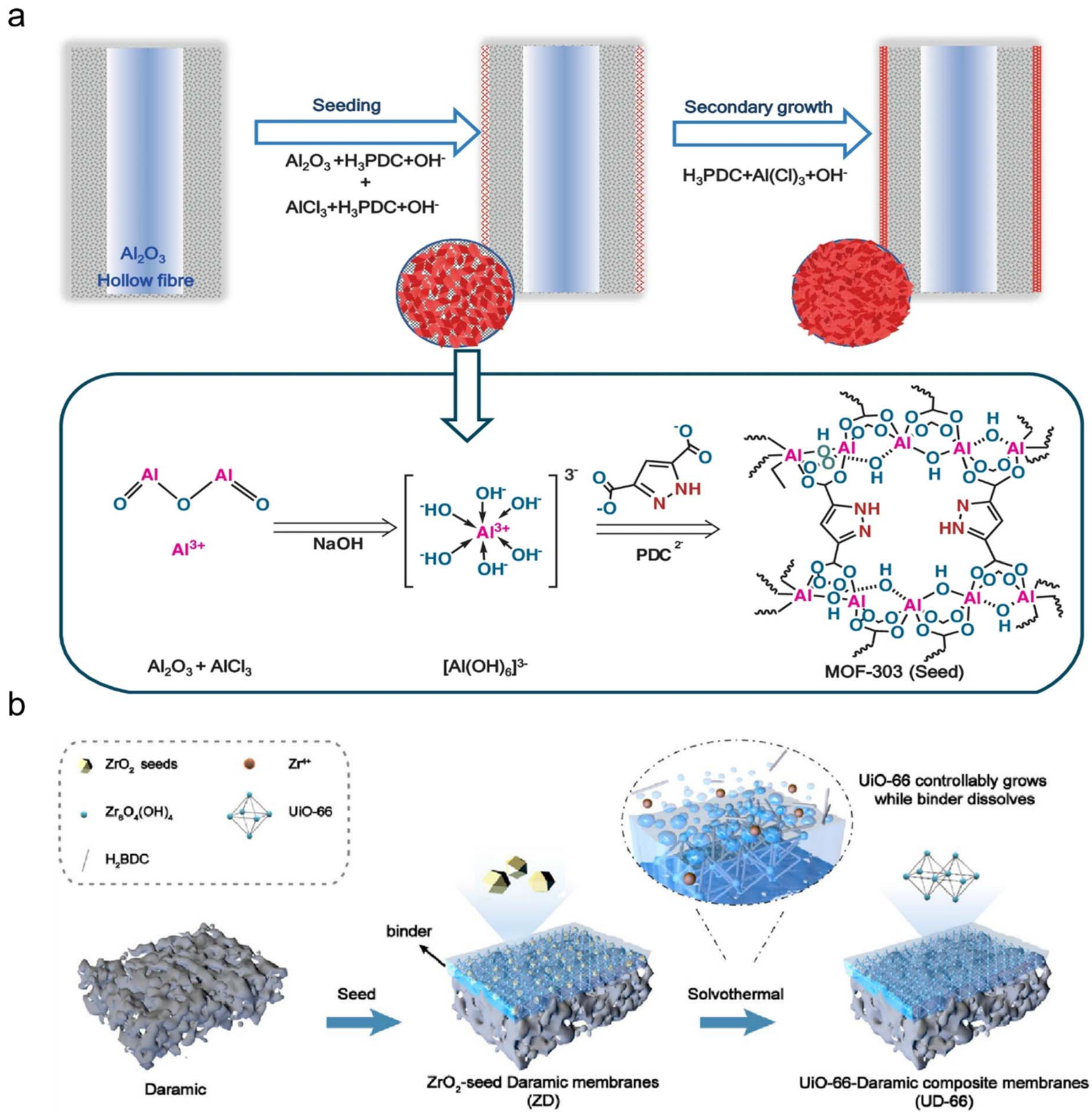

Fig. 17 (a) Bimetallic-source secondary growth strategy for MOF membrane fabrication.[198] Copyright 2024, Springer. (b) Seed-polymer blended to fabricate the substrate for MOF membrane synthesis.[201] Copyright 2021, Elsevier.

performance. Conversely, on pristine substrates, ZIF-8 crystallization occurred throughout the porous channels, which impeded the formation of a continuous membrane layer.

Kwon *et al.* innovated an *in situ* synthesis strategy directly inspired by the counter-diffusion concept.[205] In this method, a substrate saturated with a zinc salt solution was brought into contact with a solution containing a ligand and sodium formate. The key insight is that sodium formate acts as a deprotonating agent, accelerating the reaction rate to a point where it surpasses the diffusion rate. This is crucial for preventing undesired metal ion nucleation in the bulk phase. The results from this study demonstrated that the "counter-diffusion" process creates a high-concentration reaction zone at the interface. This, in combination with the catalytic effect of sodium formate, promoted the heterogeneous nucleation of crystals. An additional advantage of this approach is that crystals preferentially grow at defect sites during "counter-diffusion", effectively sealing grain boundary voids and improving the film quality.

In another example, Zhao *et al.* developed a novel approach for fabricating thiol-functionalized UiO-66 MOF channel membranes (Fig. 18b).[206] It was demonstrated that contra-diffusion synthesis on bullet-shaped PET substrates resulted in MOF membranes with asymmetric crystal growth concentrated at the tip regions. This unique morphology was directly correlated with superior ion-sieving performance. This is in sharp contrast to *in situ* grown MOF membranes on bullet-shaped PET and counter-diffusion synthesized membranes on

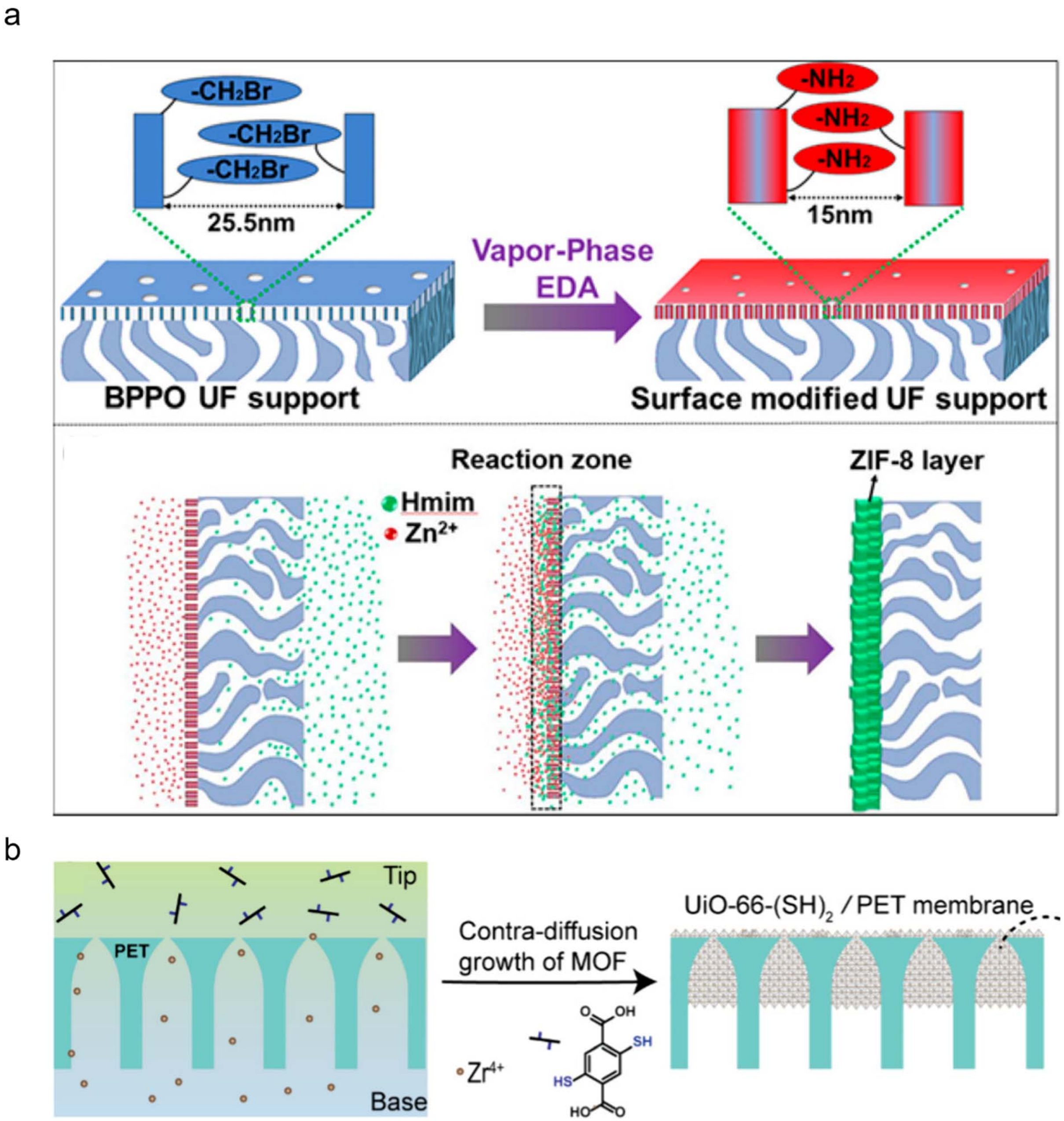

Fig. 18 (a) Schematic of ethylenediamine-modulated counter-diffusion.[204] Copyright 2016, American Chemical Society. (b) Engineering asymmetric sub-nanometer channels.[204] Copyright 2024, American Chemistry Society.

cylindrical PET, both of which showed uniform crystal distribution throughout the channels, ultimately compromising ion transport selectivity.

### 4.7 Advanced synthesis of MOF membranes

Electrochemical synthesis serves as an emerging strategy for the construction of MOF membranes. Specifically, the electric field enables directed precursor delivery and induces subsequent high-density nucleation. Wang *et al.* exemplified this by pioneering an additive-accelerated electrodeposition (AAED) methodology based on the synergistic combination of a strong electric field and a catecholamine-based additive.[207] The applied electric field drives the rapid deposition of additive–ligand complexes onto the substrate, which initiates the formation of high-density crystal nuclei. The results elucidated that the additive subsequently heals grain boundary defects during the crystal growth phase, ultimately resulting in the formation of a continuous and dense ultrathin MOF membrane.

The utilization of mixed-linker MOFs represents an effective strategy for the design of membrane asymmetric architectures, enabling the tailored engineering of both functionality and pore structure. However, organic linkers with varying reactivity often lead to deviations between the final MOF structure and the designed blueprint. To address this challenge, Zhou *et al.*

pioneered an electrochemical synthesis approach for fabricating mixed-linker MOF membranes.[208] In this case, the current intensity precisely regulated the deprotonation kinetics of the linkers, thereby stabilizing the overall deprotonation level of both ligands. Remarkably, the molar ratio of the two linkers incorporated into the MOF framework was closely aligned with the designed compositions.

While bulk MOFs can be exfoliated into nanosheets *via* solvent intercalation for subsequent membrane assembly, similar to COFs, a critical challenge is their propensity to restack randomly, creating tortuous pathways that hinder solute transport.[209] To address this, Qiu *et al.* introduced a super-spreading confinement assembly strategy to construct highly oriented MOF membranes for selective sieving capabilities.[210] The aligned stacking of nanosheets creates straight mass transfer channels, significantly reducing ion transport resistance. The results revealed that the dehydration energy barrier is higher for multivalent ions than for monovalent ions, enabling high mono-/multivalent ion selectivity. Concurrently, divalent ions exhibit distinct binding energies, which critically influence their transmembrane transport behaviors. The prepared membrane exhibited high $K^+/La^{3+}$ and $K^+/Ni^{2+}$ selectivities of 59 and 26.6, respectively, demonstrating a distinct preference for the permeation of monovalent ions.

## 5 Ion-related separations using COF/MOF membranes

Because of their intrinsic well-defined architectures, tunable pore dimensions, and long-range ordered nanochannels, COF/MOF membranes are a promising platform for high-precision ion separations. These framework-based membranes have demonstrated significant potential in a wide range of applications, including the sieving of different alkali metals in monovalent/monovalent ion separation, and the selective recovery of critical metals in mono-/multivalent ion separation, such as $Li^+/Mg^{2+}$ separation. They also show promise in water/salt separation, which includes seawater desalination and the removal of heavy metals. These capabilities enable critical mineral extraction and secondary resource recovery across diverse separation-based scenarios.

### 5.1 Desalination

The increasing global water scarcity, exacerbated by industrialization, underscores the critical role of membrane-based desalination in securing clean water.[211,212] Despite their widespread use, traditional polymeric desalination membranes exhibit an intrinsic trade-off between permeability and selectivity. This challenge arises from their highly cross-linked pore networks, which fundamentally limit their separation efficiency.[213] Conversely, MOF membranes, possessing precisely ordered nanochannels and negligible non-selective voids, present a compelling alternative for advanced desalination technologies.[214] This was exemplified by Jian *et al.*, who fabricated a laminated Al-based MOF membrane on a porous alumina substrate using a vacuum-assisted filtration method. The interlayer architecture was stabilized by strong π–π interactions, which resulted in stable operation for more than 750 hours.[215] The resulting Al-MOF membrane achieved near-complete rejection of $Na^+$, $K^+$, $Mg^{2+}$, and $Ca^{2+}$ ions (ion permeance ≈ $3.3 \times 10^{-6}$ mol m$^{-2}$ h$^{-1}$ bar$^{-1}$) while maintaining an exceptional water permeance of 2.2 mol m$^{-2}$ h$^{-1}$ bar$^{-1}$. Molecular dynamics simulations provided a mechanistic understanding of this high performance, confirming that size exclusion was the primary rejection mechanism. Specifically, the intrinsic MOF channels, with dimensions smaller than those of hydrated ions but larger than those of water molecules, enabled superior water/ion separation. Water density mapping further supported this by showing that 82.92% of water molecules preferentially permeated through the intrinsic pores of the MOF rather than the interlayer gaps.

As a burgeoning thermal-membrane coupled desalination technology, pervaporation has drawn considerable interest thanks to its outstanding water/monovalent salt selectivity.[216] Nevertheless, traditional pervaporation membranes suffer from a key drawback: their tortuous transport pathways and uncontrolled pore dimensions fundamentally limit their separation efficiency. By leveraging their programmable chemical microenvironment and designable channel architectures, COF materials represent a promising and transformative platform for advanced pervaporation systems.[188] Recently, Wang *et al.* constructed a mixed-dimensional COF membrane with remarkable structural integrity by depositing TpPa-$SO_3H$ nanosheets interconnected with TpTTPA nanoribbons on a PTFE substrate.[217] This robust architecture arises from synergistic electrostatic and π–π interactions between the two components. This ingenious design yielded a record-breaking water flux of 267 kg m$^{-2}$ h$^{-1}$ and 99.91% salt rejection in pervaporation. The exceptional water flux stems from two critical characteristics: the vertically aligned pore architecture and the presence of sulfonic acid groups embedded within the channel walls. These functional groups form hydrogen-bonded networks that trap water molecules, facilitating fast water molecular transport *via* a hopping mechanism. A quartz crystal microbalance (QCM) further supported these findings by quantitatively demonstrating a 40% enhancement in water adsorption capacity in the sulfonated COFs. This work provides a clear example of purpose-driven material engineering for advanced separation membranes.

Reverse osmosis (RO) is a desalination technique that applies external pressure to drive water permeation against the osmotic pressure. In a recent work, Sun *et al.* developed a photoresponsive COF membrane for reverse osmosis desalination using a defect-engineering strategy that incorporated spiropyran (SP) units.[218] This integration of SP enables dynamic modulation of the pore size from 6.9 Å to 4.0 Å and simultaneous alteration in the pore chemical microenvironment and hydration structure. Under UV irradiation, SP isomerization causes the membrane pores to transform into zwitterionic channels with alternating positive and negative charges. This transformation enhances electrostatic interactions with water molecules, thereby promoting the formation of a continuous hydration layer. The TAPA-TFP-SP-25% COF membrane, with an initial pore size of 6.9 Å, exhibited exceptional desalination performance, achieving 91.2% NaCl rejection. Molecular dynamics simulations further clarified the mechanism, revealing that the modified COF membranes form hydration layers with a thickness of 0.28–0.47 nm, which effectively reduces the functional pore size from 1.11 nm to 0.40 nm.

### 5.2 Heavy metal removal

Heavy metals, as representative non-biodegradable inorganic contaminants, pose critical environmental concerns. Industrial wastewater containing high concentrations of these metals presents substantial risks to biological systems and can compromise human immune function. MOFs, with their hierarchical "window-channel" architectures, are particularly well-suited for this task. The sub-nanometer windows of these structures enable precise ion sieving, while the interconnected channels facilitate water permeation. This unique architecture offers a promising route to overcome the traditional permeability–selectivity trade-off.[47]

Yuan *et al.* leveraged this strategy by dip-coating seeds onto an aluminum oxide substrate, followed by a secondary growth step to fabricate a ZIF-300 selective layer.[199] The results demonstrated that their separation performance was independent of the charge characteristics of the solutes. Instead, the superior rejection of heavy metal ions, whose hydrated size exceeded the pore window (7.9 Å), is consistent with theoretical predictions. Furthermore, the membrane maintained a stable permeance of 39.2 LMH bar$^{-1}$ and 99.21% rejection for $CuSO_4$ during 12-hour crossflow operation. The ZIF-300 membrane also retained its structural integrity after immersion in water for 30 days, highlighting its practical potential for sustainable water management.

COF membranes, featuring tunable pore dimensions and chemical microenvironments, are garnering increasing attention for selective heavy metal separation. Zheng *et al.* advanced this field with an innovative strategy that combined pore-size engineering and charge reversal. Their method involved the vacuum-assisted self-assembly of Tp-$SO_3H$ nanosheets on a PAN substrate, followed by a polyelectrolyte dip-coating step.[219] This PEI coating was instrumental, reducing the effective pore size from 0.78 nm to 0.60 nm and simultaneously reversing the membrane surface potential from −40 mV to +31 mV. This dual modification synergistically reinforced both size exclusion and electrostatic repulsion, promoting highly efficient cation rejection. The modified COF membranes achieve rejection rates of 98.5% for $Cr^{3+}$, 97.3% for $Cd^{2+}$, 97.0% for $Pb^{2+}$, 96.2% for $Cu^{2+}$, and 96.0% for $Ni^{2+}$ ions, respectively. These high rejection rates were sustained above 95% throughout a continuous 7-day operation, and the universality of the approach was confirmed by the robust rejection performance of membranes modified with both PDDA and PAH.

### 5.3 Lithium extraction

Technological advancements drive the energy revolution, while simultaneously posing a critical challenge: securing the lithium supply essential for the emerging new energy sector.[220] In this context, membrane-based lithium extraction has emerged as a promising, eco-friendly, and highly efficient solution. A key challenge, however, is the need for membranes to selectively permeate lithium ions while effectively rejecting competing ions, such as magnesium and other monovalent ions with similar properties.[221] This requirement is distinct from traditional desalination or heavy metal removal. Despite the low energy consumption of membrane-based lithium extraction, conventional polymer membranes are often unsuitable due to their overly cross-linked and poorly tunable pore structures, which fundamentally constrain both extraction efficiency and the elucidation of $Li^+$ transport mechanisms. The advent of COF/MOF membranes, with their precise and programmable architectures, presents a new frontier for this application.

Wu *et al.* created a negatively charged, N-rich 3D COF membrane that enables strong electrostatic adsorption of cations.[169] This membrane demonstrated significantly higher permeance for monovalent ions compared to divalent ions, achieving a $Li^+/Mg^{2+}$ selectivity of 36 in mixed feed solutions. The observed ion differentiation behavior is attributed to both size sieving effects and ion–channel interactions. Their intrinsic pore size of approximately 7.8 Å lies between the hydrated diameters of $Li^+$ and $Mg^{2+}$ ions. This enables the free transport of $Li^+$ ions while requiring divalent metal ions to undergo a high-energy partial dehydration process for permeation. Furthermore, the strong electrostatic affinity between the nitrogen atoms and $Mg^{2+}$ ions contributes to the high selectivity. The potential of COF membranes for practical lithium extraction was highlighted by their exceptional physicochemical stability, maintaining a separation factor higher than 12 across 10 operational cycles in high-$Mg^{2+}/Li^+$ ratio simulated brines.

Biomimetic innovation in highly selective membranes is predicated on intricate solvation and coordination interactions between target substances and membrane channels.[85] Meng *et al.* exemplified this by using reticular chemistry to create a series of structurally similar COF membranes with varying side chains.[222] By precisely controlling the length of the oligoether chains, they successfully tuned the membrane solvation capability, thereby affecting ion transport behaviors. The mechanism relies on oxygen atoms in the oligoether chains forming coordination bonds with ions, replacing their original hydration shells to facilitate ion permeation. The pronounced flexibility of the extended oligoether chains further enables conformational adaptation to aid ion transport. However, it was found that excessive chain length compromises ion selectivity by occupying free volume and creating overly strong interactions. The COF–$EO_2$ membrane, featuring two ethylene oxide units, achieved optimal solvation capability. This maximized the energy barrier difference between $Li^+$ and $Mg^{2+}$, leading to an exceptional $Li^+/Mg^{2+}$ separation factor of 1352 under electro-driven conditions. This work establishes solvation capability as a crucial design principle for membrane materials and highlights the importance of competitive binding in confined spaces for ion transport. In parallel, Ren *et al.* developed an on-demand nanochannel construction strategy by assembling COF nanosheets grafted with oligoethers (OEs).[223] The introduced OEs tuned the COF pore size to lie between the hydrated radii of $Li^+$

and $Mg^{2+}$ ions, resulting in a higher dehydration energy barrier for $Mg^{2+}$ than for $Li^+$. Concurrently, the oxygen atoms of the OEs formed dynamic Li–O bonds with partially dehydrated $Li^+$ ions, facilitating rapid $Li^+$ transport through continuous bond formation and dissociation within the pores. Furthermore, the positively charged nanosheets exerted stronger electrostatic repulsion toward the highly charged $Mg^{2+}$, further enhancing $Li^+/Mg^{2+}$ selectivity. The resulting COF membrane achieved a $Li^+/Mg^{2+}$ separation factor of 30.2 and a water permeability of 32.1 L $m^{-2}$ $h^{-1}$ $bar^{-1}$.

Azobenzene serves as a prototypical molecular photoswitch, widely employed in the bio-inspired design of functional materials.[224] Expanding on this, Ren *et al.* introduced a biomimetic nanochannel modulation (BNM) strategy to construct an intelligent COF membrane decorated with azobenzene derivatives.[225] This membrane demonstrated superior ion-sieving performance, with ideal selectivities of 17.9 for $K^+/Li^+$ and 24.9 for $Li^+/Mg^{2+}$. In this case, the hydroxyl groups on the DHTP linker served as grafting sites for the azobenzene moieties, whose density was precisely tuned by varying the DHTP ratio. The incorporation of azobenzene not only enabled precise pore size control, reducing it from 2.73 nm to 1.58 nm, but also conferred photoresponsiveness, allowing angstrom-level pore switching (from 1.58 nm to 1.64 nm) upon light irradiation. Furthermore, the study revealed the critical influence of the azobenzene substituent on the nanochannel performance. The results elucidated that the sulfonic acid group, with the strongest dissociative ability, provided more water-binding sites, forming the thickest hydration layer and resulting in an effective pore size of approximately 7.4 Å.

### 5.4 Rare earth metal separation

Rare earth elements are critical strategic resources due to their supply chain vulnerabilities and their essential role in digital infrastructure.[226] Membrane-based rare earth extraction represents a promising green technology for both primary ore extraction and secondary resource recovery.[227] As an emerging material platform, COF membranes represent a transformative solution due to their ability to construct precise sub-nanochannels. This positions COF membranes as an ideal platform for the high-precision extraction of rare earth elements, a task crucial for maximizing resource efficiency.[73]

A key advance was demonstrated by Shi *et al.*, who constructed a TFPM-EB selective layer on a cross-linked polyimide (CPI) substrate to create a COF membrane for rare earth separation.[228] The resulting membrane displayed exceptional ion selectivity in single-component tests, with a water flux of 23.2 LMH $bar^{-1}$ and remarkable rejection values of 91.4% for $La^{3+}$, 53.4% for $Sr^{2+}$, and only 2.4% for $Cs^+$. It was concluded that the differential ion transport behavior was primarily governed by size exclusion due to the almost neutral membrane surface. Specifically, the membrane—with a pore diameter of approximately 0.70–0.86 nm—exhibited moderate rejection toward hydrated $Sr^{2+}$ ions (0.82 nm), high rejection of the larger hydrated $La^{3+}$ ions (0.90 nm), and permitted permeation of the smaller hydrated $Cs^+$ ions (0.66 nm).

However, the difference in ionic radii of rare earth elements is merely 0.18 Å, significantly smaller than that observed for other transition metal ions.[229] This minimal variance renders them particularly challenging to separate *via* conventional size-sieving methods. Previous investigations have demonstrated that incorporating high-affinity REE-binding ligands within COFs enables effective sequestration of these strategic metals.[230] Expanding on this, Deng *et al.* innovated a Janus 2D COF membrane that leverages precise positioning of functional groups to boost coordination for efficient rare earth metal separation.[231] The *ortho*-hydroxyl configured COF membrane proved to be exceptionally selective for Sr(II) (99.7%) and maintained over 95.8% selectivity across 5 reuse cycles. This performance was in stark contrast to the *para*-hydroxyl variant, which achieved only 66.4% selectivity. A deeper understanding of the mechanism was provided by DFT calculations, which showed a substantially stronger Y(III) binding energy for the *ortho*-configuration (−63.6 kcal $mol^{-1}$) compared to the *para*-configuration (−24.4 kcal $mol^{-1}$). This performance difference highlights how enhanced coordination between Y(III) ions and strategically positioned O/N atoms in the *ortho*-hydroxyl framework drives superior Sr/Y separation.

## 6 Conclusion and outlook

The urgent global challenges in ecological security and resource sustainability underscore the critical need for green and efficient ion separation technologies. This review addresses this imperative by focusing on fundamental ion transport mechanisms within sub-nanometer channels, the key design strategies for crystalline covalent organic frameworks (COFs) and metal–organic frameworks (MOFs), and advanced methodologies for fabricating high-performance membranes. We further explore the diverse applications of these ion-selective COF/MOF membranes, offering a comprehensive theoretical and practical framework to guide future material development and process optimization. While significant progress has been made in creating ultrathin, continuous, and defect-free membranes, persistent challenges highlight promising new directions for research.

(1) The intricate behavior of ion transport within MOF/COF membranes stems from the synergistic interplay of steric hindrance, dehydration effects, and specific ion–pore interactions. This complexity necessitates precise control over pore architecture, the local chemical environment, and pore wall hydrophilicity/hydrophobicity. Specifically, the remarkable flexibility of COF/MOF materials inspires innovative design strategies such as engineering heterogeneous channels, asymmetric architectures, and amphiphilic nanochannels. Concurrently, insights from biomimetic ion channels reveal the profound influence of ion–ion and ion–pore interactions at the sub-nanometer scale. In this context, a critical future research direction lies in integrating multiscale characterization with computational modeling to comprehensively unravel the intricate interactions among active sites, target ions, and competing species—an approach that will pave the way for the rational design of next-generation, highly selective framework-based membranes.

(2) While COF/MOF materials offer a novel pathway to transcend the traditional permeability–selectivity trade-off of conventional membranes, significant obstacles in their synthesis persist. Current synthesis strategies suffer from critical limitations: continuous COF membrane growth generally requires elevated temperatures or specific catalytic systems, while MOF fabrication approaches—such as surface modification to suppress heterogeneous nucleation—are often complex, lack broad applicability, and are restricted to a narrow range of substrates and MOF types. Moreover, universal scalability barriers, including the high cost of molecular building blocks, weak interfacial adhesion, and harsh reaction conditions, further exacerbate these challenges. Addressing these issues urgently calls for the development of novel, versatile, and low-cost methods for fabricating ultrathin COF/MOF membranes. Establishing a more mature theoretical framework is equally essential, requiring research that quantitatively elucidates the influence of process parameters on physicochemical properties and, crucially, defines clear structure–performance relationships for COF/MOF-based separations.

(3) To enhance the separation efficiency and broaden applicability, the future design of ion-selective COF/MOF membranes should incorporate multifunctionality—such as intrinsic antimicrobial properties to mitigate biofouling, or catalytic sites for surface-level decontamination. Furthermore, the engineering of stimuli-responsive frameworks offers a sophisticated route for precision separation, enabling reversible modulation of pore size or chemical properties to achieve high-precision separation of multi-component systems.

(4) The selection of building blocks and optimization of synthesis conditions for COF/MOF membranes often rely on experimental intuition or trial-and-error methods, which limits development efficiency. Machine learning emerges as a powerful tool to accelerate the rational design of materials, significantly reducing time-consuming empirical approaches. In addition, adopting green synthesis methodologies—such as using deep eutectic solvents, bio-derived building blocks, aqueous two-phase systems, and microwave-assisted synthesis—is crucial to address the environmental and economic sustainability challenges in production. These represent urgent and essential directions for the future development of COF/MOF membranes.

## Author contributions

Penglin Cheng: conceptualization, writing – original draft. Tiantian Chen, Tiantian Liu, and Yuhan Wei: investigation, visualization. Junyong Zhu, Miaomiao Tian, Yatao Zhang, and Bart Van der Bruggen: supervision, writing – review & editing. Xueli Cao and Shi-Peng Sun: project administration.

## Conflicts of interest

The authors declare that they have no known competing financial interests or personal relationships that could have appeared to influence the work reported in this paper.

## Data availability

Data availability is not applicable to this article as no new data were created or analyzed in this study.

## Acknowledgements

This work was supported by the Major Research Plan of the National Natural Science Foundation of China (92475120, 52573238), the Outstanding Youth Fund of the Henan Scientific Committee (252300421182), and the Jiangsu Future Membrane Technology Innovation Center (BM2021804).

## References

1 P. S. Goh, K. C. Wong and A. F. Ismail, *Desalination*, 2022, **521**, 115377.
2 O. Lefebvre and R. Moletta, *Water Res.*, 2006, **40**, 3671–3682.
3 J. Thorslund, M. F. P. Bierkens, G. H. P. Oude Essink, E. H. Sutanudjaja and M. T. H. van Vliet, *Nat. Commun.*, 2021, **12**, 4232.
4 G. Lin, B. Zeng, J. Li, Z. Wang, S. Wang, T. Hu and L. Zhang, *Chem. Eng. J.*, 2023, **460**, 141710.
5 F. Zhu, Y.-M. Zheng, B.-G. Zhang and Y.-R. Dai, *J. Hazard. Mater.*, 2021, **401**, 123608.
6 N. N. R. Ahmad, W. L. Ang, C. P. Leo, A. W. Mohammad and N. Hilal, *Desalination*, 2021, **517**, 115170.
7 S. Bolisetty, M. Peydayesh and R. Mezzenga, *Chem. Soc. Rev.*, 2019, **48**, 463–487.
8 J. Xu, Y. Jin, K. Liu, N. Lyu, Z. Zhang, B. Sun, Q. Jin, H. Lu, H. Tian, X. Guo, D. Shanmukaraj, H. Wu, M. Li, M. Armand and G. Wang, *Sci. Adv.*, 2022, **8**, eabq7948.
9 H. Jin, Y. Hu, Z. Shen, H. Pan, H. Bao, L. Yin, G. Zhao, Z. Ji, X. Wang and X. Huang, *Nat. Commun.*, 2025, **16**, 3574.
10 S. Liu, Q. Sun, N. Xu, Y. Wang, Y. Li, J. Li, Z. Li, V. D. Rajput, T. Minkina, X. Kong, G. Li, Y. Lin, Y. Zhao and X. Duan, *Coord. Chem. Rev.*, 2025, **523**, 216268.
11 W. Shi, J. Li, F. Gao, L. Meng, X. Su and Z. Wang, *Nat. Commun.*, 2024, **15**, 10828.
12 S. Wan, W.-J. Liu, G. Tan and H.-Q. Yu, *Proc. Natl. Acad. Sci.*, 2025, **122**, e2423217122.
13 J. Yang, Y. Wang, M. Zhang, P. Wang, X. He, H. Zhou and P. He, *Angew. Chem., Int. Ed.*, 2024, **63**, e202411957.
14 V. Balaram, M. Santosh, M. Satyanarayanan, N. Srinivas and H. Gupta, *Geosci. Front.*, 2024, **15**, 101868.
15 H. Nikkhah, D. Ipekçi, W. Xiang, Z. Stoll, P. Xu, B. Li, J. R. McCutcheon and B. Beykal, *Chem. Eng. J.*, 2024, **498**, 155349.
16 H. Peng, K. Yu, X. Liu, J. Li, X. Hu and Q. Zhao, *Nat. Commun.*, 2023, **14**, 5483.
17 F. Soyekwo, C. Liu, X. Mao and X. Shi, *Adv. Funct. Mater.*, 2025, **35**, 2412463.
18 S. Yang, Y. Wang, H. Pan, P. He and H. Zhou, *Nature*, 2024, **636**, 309–321.
19 Y. L. Xue, J. Huang, C. H. Lau, B. Cao and P. Li, *Nat. Commun.*, 2020, **11**, 1461.

20 D.-Y. Koh, B. A. McCool, H. W. Deckman and R. P. Lively, *Science*, 2016, **353**, 804–807.
21 S. Han, J. Zhu, A. A. Uliana, D. Li, Y. Zhang, L. Zhang, Y. Wang, T. He and M. Elimelech, *Nat. Commun.*, 2022, **13**, 7954.
22 R. Xu, X. Xiao, G. Zhang, Y. Ye, P. Zhang, Y. Yang, S. B. Shuchi and Y. Cui, *Matter*, 2024, **7**, 3876–3890.
23 L. F. Villalobos, J. Zhang and M. Elimelech, *One Earth*, 2023, **6**, 767–771.
24 Y. Yao, P. Zhang, F. Sun, W. Zhang, M. Li, G. Sha, L. Teng, X. Wang, M. Huo, R. M. DuChanois, T. Cao, C. Boo, X. Zhang and M. Elimelech, *Science*, 2024, **384**, 333–338.
25 L. Ren, H. Wu, J. Han and J. Chen, *Adv. Funct. Mater.*, 2025, 2425244.
26 Z.-J. Fu, S.-K. Jiang, X.-Y. Chao, C.-X. Zhang, Q. Shi, Z.-Y. Wang, M.-L. Liu and S.-P. Sun, *Water Res.*, 2022, **222**, 118888.
27 P. Gozali Balkanloo, A. Poursattar Marjani and M. Mahmoudian, *Chem. Eng. J.*, 2024, **496**, 153835.
28 F. Fan, Y. Ren, S. Zhang, Z. Tang, J. Wang, X. Han, Y. Yang, G. Lu, Y. Zhang, L. Chen, Z. Wang, K. Zhang, J. Gao, J. Zhao, G. Cui and B. Tang, *Adv. Sci.*, 2024, **11**, 2402898.
29 Z. H. Foo, D. Rehman, A. T. Bouma, S. Monsalvo and J. H. Lienhard, *Environ. Sci. Technol.*, 2023, **57**, 6320–6330.
30 Z. Lv, X. Zhang, Q. Gao, C. Wen, Y. He, H. Tan, L. Qian, W. Qi, X. Chen and Z. Li, *Adv. Funct. Mater.*, 2024, **34**, 2409274.
31 M. Qiu, Z. Zhu, D. Wang, Z. Xu, W. Miao, L. Jiang and Y. Tian, *J. Am. Chem. Soc.*, 2023, **145**, 12275–12283.
32 D. Li, W. Liu, X. Wang, W. Lin, J. Zhai, H. Fan, K. Xiao, K. Wang, Y. Li, Y. Jin, J. Fang, Y. Shen, M. Elimelech and X. Huang, *Sci. Adv.*, 2025, **11**, eadt3324.
33 Z. Song, Z. Wang, Y. Yang, J. Zhang, W. Fang and J. Jin, *Chem. Eng. J.*, 2025, **505**, 159637.
34 Y. Liu, W. Fang, Z. Yue, Y. Wang, Y. Zhu, J. Jin and L. Jiang, *Nat. Water*, 2025, **3**, 430–438.
35 O. M. Yaghi, *J. Am. Chem. Soc.*, 2016, **138**, 15507–15509.
36 H. Jiang, D. Alezi and M. Eddaoudi, *Nat. Rev. Mater.*, 2021, **6**, 466–487.
37 S. J. Rowan, S. J. Cantrill, G. R. L. Cousins, J. K. M. Sanders and J. F. Stoddart, *Angew. Chem., Int. Ed.*, 2002, **41**, 898–952.
38 Z. Lei, H. Chen, S. Huang, L. J. Wayment, Q. Xu and W. Zhang, *Chem. Rev.*, 2024, **124**, 7829–7906.
39 S. Maes, N. Badi, J. M. Winne and F. E. Du Prez, *Nat. Rev. Chem.*, 2025, **9**, 144–158.
40 P. Z. Moghadam, Y. G. Chung and R. Q. Snurr, *Nat. Energy*, 2024, **9**, 121–133.
41 Y.-H. Jin, M.-H. Li and Y.-W. Yang, *Adv. Sci.*, 2025, **12**, 2412600.
42 M. Åhlén, X. Kong, W. Zhao, F. Zamora and C. Xu, *Angew. Chem., Int. Ed.*, 2025, e202425426.
43 D. N. Ampong, E. Effah, E. A. Tsiwah, A. Kumar, E. Agyekum, E. N. A. Doku, O. Issaka, F. O. Agyemang, K. Mensah-Darkwa and R. K. Gupta, *Coord. Chem. Rev.*, 2024, **519**, 216121.
44 Y. Du, D. Lei, X. Hao, Z. Liu and X. Du, *Sep. Purif. Technol.*, 2025, **376**, 133979.
45 W. Meng, S. Chen, Z. Guo, F. Gao, J. Wang, J. Lu, Y. Hou, Q. He, X. Zhan, M. Qiu and Q. Zhang, *Nat. Water*, 2025, **3**, 191–200.
46 N. Stock and S. Biswas, *Chem. Rev.*, 2012, **112**, 933–969.
47 M. S. Denny, J. C. Moreton, L. Benz and S. M. Cohen, *Nat. Rev. Mater.*, 2016, **1**, 16078.
48 R.-R. Liang, S. Xu, Z. Han, Y. Yang, K.-Y. Wang, Z. Huang, J. Rushlow, P. Cai, P. Samorì and H.-C. Zhou, *J. Am. Chem. Soc.*, 2024, **146**, 9811–9818.
49 R. C. Rohde, K. M. Carsch, M. N. Dods, H. Z. H. Jiang, A. R. McIsaac, R. A. Klein, H. Kwon, S. L. Karstens, Y. Wang, A. J. Huang, J. W. Taylor, Y. Yabuuchi, N. V. Tkachenko, K. R. Meihaus, H. Furukawa, D. R. Yahne, K. E. Engler, K. C. Bustillo, A. M. Minor, J. A. Reimer, M. Head-Gordon, C. M. Brown and J. R. Long, *Science*, 2024, **386**, 814–819.
50 R.-R. Liang, Z. Liu, Z. Han, Y. Yang, J. Rushlow and H.-C. Zhou, *Angew. Chem., Int. Ed.*, 2025, **64**, e202414271.
51 X. Zhou, X. Chen, B. Yang, S. Luo, M. Guo, N. An, H. Tian, X. Li and J. Shao, *Adv. Funct. Mater.*, 2025, 2501683.
52 P. Das, G. Chakraborty, J. Kaur and S. K. Mandal, *Small*, 2025, **21**, 2408810.
53 M. Abdollahzadeh, M. Chai, E. Hosseini, M. Zakertabrizi, M. Mohammad, H. Ahmadi, J. Hou, S. Lim, A. Habibnejad Korayem, V. Chen, M. Asadnia and A. Razmjou, *Adv. Mater.*, 2022, **34**, 2107878.
54 L. A. Richards, A. I. Schäfer, B. S. Richards and B. Corry, *Small*, 2012, **8**, 1701–1709.
55 Z. Chen, C. Hu, C. Lu, J. Sun, Y. Zhang, F. Wang and J. Qu, *ACS Nano*, 2023, **17**, 12629–12640.
56 C. Lu, C. Hu, C. L. Ritt, X. Hua, J. Sun, H. Xia, Y. Liu, D.-W. Li, B. Ma, M. Elimelech and J. Qu, *J. Am. Chem. Soc.*, 2021, **143**, 14242–14252.
57 L. Hou, W. Xian, S. Bing, Y. Song, Q. Sun, L. Zhang and S. Ma, *Adv. Funct. Mater.*, 2021, **31**, 2009970.
58 C. Violet, A. Ball, M. Heiranian, L. F. Villalobos, J. Zhang, B. Uralcan, H. Kulik, A. Haji-Akbari and M. Elimelech, *Nat. Water*, 2024, **2**, 706–718.
59 S. Babu M K, Y.-S. Yun and S. Kancharla, *Coord. Chem. Rev.*, 2024, **507**, 215699.
60 G. M. Jaid, A. A. AbdulRazak, H. Meskher, S. Al-Saadi and Q. F. Alsalhy, *Mater. Today Sustain.*, 2024, **25**, 100672.
61 S.-Q. Cheng, Y. Liu and Y. Sun, *Coord. Chem. Rev.*, 2025, **534**, 216559.
62 P. Marchetti, M. F. Jimenez Solomon, G. Szekely and A. G. Livingston, *Chem. Rev.*, 2014, **114**, 10735–10806.
63 Y. Yang, L. Yu, T. Chu, H. Niu, J. Wang and Y. Cai, *Nat. Commun.*, 2022, **13**, 2615.
64 T. Xu, B. Wu, L. Hou, Y. Zhu, F. Sheng, Z. Zhao, Y. Dong, J. Liu, B. Ye, X. Li, L. Ge, H. Wang and T. Xu, *J. Am. Chem. Soc.*, 2022, **144**, 10220–10229.
65 L. Huang, H. Wu, L. Ding, J. Caro and H. Wang, *Angew. Chem., Int. Ed.*, 2024, **63**, e202314638.
66 Y. Xue, Y. Xia, S. Yang, Y. Alsaid, K. Y. Fong, Y. Wang and X. Zhang, *Science*, 2021, **372**, 501–503.

67 H. Zhang, J. Hou, Y. Hu, P. Wang, R. Ou, L. Jiang, J. Z. Liu, B. D. Freeman, A. J. Hill and H. Wang, *Sci. Adv.*, 2018, **4**, eaaq0066.

68 A. Razmjou, M. Asadnia, E. Hosseini, A. Habibnejad Korayem and V. Chen, *Nat. Commun.*, 2019, **10**, 5793.

69 S. Hong, F. Al Marzooqi, J. K. El-Demellawi, N. Al Marzooqi, H. A. Arafat and H. N. Alshareef, *ACS Mater. Lett.*, 2023, **5**, 341–356.

70 S. Xu, H. Lin, G. Li, Q. Han, J. Wang and F. Liu, *Adv. Sci.*, 2024, **11**, 2405539.

71 R. Xu, Y. Kang, W. Zhang, X. Zhang and B. Pan, *Angew. Chem., Int. Ed.*, 2022, **61**, e202115443.

72 W. Kopec, D. A. Köpfer, O. N. Vickery, A. S. Bondarenko, T. L. C. Jansen, B. L. de Groot and U. Zachariae, *Nat. Chem.*, 2018, **10**, 813–820.

73 Q. Liu, M. Liu, Z. Zhang, C. Yin, J. Long, M. Wei and Y. Wang, *Nat. Commun.*, 2024, **15**, 9221.

74 H. Wang, Y. Zhai, Y. Li, Y. Cao, B. Shi, R. Li, Z. Zhu, H. Jiang, Z. Guo, M. Wang, L. Chen, Y. Liu, K.-G. Zhou, F. Pan and Z. Jiang, *Nat. Commun.*, 2022, **13**, 7123.

75 T. Cao, L. Wang, K. E. Pataroque, R. Wang and M. Elimelech, *Environ. Sci. Technol.*, 2025, **59**, 5819–5828.

76 Y. Guo, J. He, J. Zhang, M. Sheng, Z. Wang, M. Elimelech and L. Wang, *Sci. Adv.*, 2025, **11**, eadu8302.

77 X. You, L. Cao, Y. Liu, H. Wu, R. Li, Q. Xiao, J. Yuan, R. Zhang, C. Fan, X. Wang, P. Yang, X. Yang, Y. Ma and Z. Jiang, *ACS Nano*, 2022, **16**, 11781–11791.

78 J. Lu, H. Zhang, J. Hou, X. Li, X. Hu, Y. Hu, C. D. Easton, Q. Li, C. Sun, A. W. Thornton, M. R. Hill, X. Zhang, G. Jiang, J. Z. Liu, A. J. Hill, B. D. Freeman, L. Jiang and H. Wang, *Nat. Mater.*, 2020, **19**, 767–774.

79 W. Meng, S. Chen, M. Wu, F. Gao, Y. Hou, X. Zhan, W. Hu, L. Liang and Q. Zhang, *Angew. Chem., Int. Ed.*, 2025, **64**, e202422423.

80 K. Liu, R. Epsztein, S. Lin, L. Liu, J. Qu and M. Sun, *Sci. Adv.*, 2025, **11**, eadv0174.

81 W. Li, T. Xu, F. Sheng, Y. Wang, Y. Li, Y. Xia, B. Wu, X. Li and T. Xu, *J. Membr. Sci.*, 2024, **703**, 122829.

82 Z.-Q. Wu, C.-Y. Li, X.-L. Ding, Z.-Q. Li and X.-H. Xia, *J. Phys. Chem. Lett.*, 2022, **13**, 5267–5274.

83 D. Zou and Y. M. Lee, *Prog. Polym. Sci.*, 2022, **128**, 101535.

84 B. Bolto, T. Tran, M. Hoang and Z. Xie, *Prog. Polym. Sci.*, 2009, **34**, 969–981.

85 R. M. DuChanois, M. Heiranian, J. Yang, C. J. Porter, Q. Li, X. Zhang, R. Verduzco and M. Elimelech, *Sci. Adv.*, 2022, **8**, eabm9436.

86 C. Jiang, S. Bai, J. Li, M. Wang, Y. Zhou and Y. Hou, *J. Membr. Sci.*, 2025, **714**, 123372.

87 T. Kanagasundaram, O. Murphy, M. N. Haji and J. J. Wilson, *Coord. Chem. Rev.*, 2024, **509**, 215727.

88 S. Bing, W. Xian, S. Chen, Y. Song, L. Hou, X. Liu, S. Ma, Q. Sun and L. Zhang, *Matter*, 2021, **4**, 2027–2038.

89 X. Li, H. Zhang, J. Hou, R. Ou, Y. Zhu, C. Zhao, T. Qian, C. D. Easton, C. Selomulya, M. R. Hill and H. Wang, *J. Am. Chem. Soc.*, 2020, **142**, 9827–9833.

90 D. Yu, X. Xiao, C. Shokoohi, Y. Wang, L. Sun, Z. Juan, M. J. Kipper, J. Tang, L. Huang, G. S. Han, H. S. Jung and J. Chen, *Adv. Funct. Mater.*, 2023, **33**, 2211983.

91 L. Cao, I. C. Chen, Z. Li, X. Liu, M. Mubashir, R. A. Nuaimi and Z. Lai, *Nat. Commun.*, 2022, **13**, 7894.

92 F. Sheng, B. Wu, X. Li, T. Xu, M. A. Shehzad, X. Wang, L. Ge, H. Wang and T. Xu, *Adv. Mater.*, 2021, **33**, 2104404.

93 X. Feng, X. Ding and D. Jiang, *Chem. Soc. Rev.*, 2012, **41**, 6010–6022.

94 S.-Y. Ding and W. Wang, *Chem. Soc. Rev.*, 2013, **42**, 548–568.

95 C. Qian, W. L. Teo, Q. Gao, H. Wu, Y. Liao and Y. Zhao, *Mater. Today*, 2023, **71**, 91–107.

96 A. P. Côté, A. I. Benin, N. W. Ockwig, M. O'Keeffe, A. J. Matzger and O. M. Yaghi, *Science*, 2005, **310**, 1166–1170.

97 Z. Liu, K. Zhang, G. Huang, B. Xu, Y.-l. Hong, X. Wu, Y. Nishiyama, S. Horike, G. Zhang and S. Kitagawa, *Angew. Chem., Int. Ed.*, 2022, **61**, e202110695.

98 Y. Kong, B. Lyu, C. Fan, Y. Yang, X. Wang, B. Shi, J. Jiang, H. Wu and Z. Jiang, *J. Am. Chem. Soc.*, 2023, **145**, 27984–27992.

99 W. Chen, Q. Liu, B. Pang, F. Cui, L. Wang, F. Zhou, G. He and X. Wu, *Small*, 2025, **21**, 2407260.

100 T. Liu, Y. Zhang, Z. Shan, M. Wu, B. Li, H. Sun, G. Su, R. Wang and G. Zhang, *Nat. Water*, 2023, **1**, 1059–1067.

101 A. Jrad, M. A. Olson and A. Trabolsi, *Chem*, 2023, **9**, 1413–1451.

102 Y. Zhang, H. Wang, W. Wang, Z. Zhou, J. Huang, F. Yang, Y. Bai, P. Sun, J. Ma, L. E. Peng, C. Y. Tang and L. Shao, *Matter*, 2024, **7**, 1406–1439.

103 T.-Y. Zhou, S.-Q. Xu, Q. Wen, Z.-F. Pang and X. Zhao, *J. Am. Chem. Soc.*, 2014, **136**, 15885–15888.

104 N. Huang, P. Wang and D. Jiang, *Nat. Rev. Mater.*, 2016, **1**, 16068.

105 M. S. Lohse and T. Bein, *Adv. Funct. Mater.*, 2018, **28**, 1705553.

106 Y. Peng, L. Li, C. Zhu, B. Chen, M. Zhao, Z. Zhang, Z. Lai, X. Zhang, C. Tan, Y. Han, Y. Zhu and H. Zhang, *J. Am. Chem. Soc.*, 2020, **142**, 13162–13169.

107 X. Hu, Z. Li, J. Li, C. Jin, J. Bao, X. Zhang, X. Jiang, N. Zhang and G. He, *Small*, 2025, **21**, 2406693.

108 J. Li, W. Lyu, X. Mi, C. Qian, Y. Liu, J. Yu, R. B. Kaner and Y. Liao, *Adv. Sci.*, 2024, **11**, 2401966.

109 S. Sun, C.-Q. Han, J.-X. Guo, L. Wang, Z.-Y. Wang, G. Lu and X.-Y. Liu, *J. Mater. Chem. C*, 2025, **13**, 2814–2821.

110 S.-Y. Jiang, Z.-B. Zhou, S.-X. Gan, Y. Lu, C. Liu, Q.-Y. Qi, J. Yao and X. Zhao, *Nat. Commun.*, 2024, **15**, 698.

111 L. Wei, S. Wu, C. Li, C. Liu, H. Chen, Y.-B. Zhang, F. Zheng, Y. Ma and Y. Zhao, *J. Am. Chem. Soc.*, 2024, **146**, 31384–31390.

112 C. E. Pelkowski, A. Natraj, C. D. Malliakas, D. W. Burke, M. I. Bardot, Z. Wang, H. Li and W. R. Dichtel, *J. Am. Chem. Soc.*, 2023, **145**, 21798–21806.

113 K. Geng, T. He, R. Liu, S. Dalapati, K. T. Tan, Z. Li, S. Tao, Y. Gong, Q. Jiang and D. Jiang, *Chem. Rev.*, 2020, **120**, 8814–8933.

114 E. L. Spitler, B. T. Koo, J. L. Novotney, J. W. Colson, F. J. Uribe-Romo, G. D. Gutierrez, P. Clancy and W. R. Dichtel, *J. Am. Chem. Soc.*, 2011, **133**, 19416–19421.
115 X. Wu, X. Han, Y. Liu, Y. Liu and Y. Cui, *J. Am. Chem. Soc.*, 2018, **140**, 16124–16133.
116 X. Tian, H. Huan, K. Zhang, R. Zhang, L. Liu, X. Liu, X. Zhang, Y. Yu, T. Gu, S. Wang and Z. Jiang, *Adv. Mater.*, 2025, 2504622.
117 D. Rana and T. Matsuura, *Chem. Rev.*, 2010, **110**, 2448–2471.
118 J. Liu, M. Peng, L. Chen, T. Li, B. Liu, D. Zhao, Z. Wang, J. Ma, H. Chu and C. Y. Tang, *Environ. Sci. Technol.*, 2025, **59**, 16056–16065.
119 M. Zhou, J. Zhou, L. Yan, S. Li, X. Cao, Y. Zhang, J. Ma, L. Shao, Z. Xie and X. Cheng, *Small*, 2025, **21**, 2505330.
120 L. Ren, H. Wu, J. Han and J. Chen, *Adv. Funct. Mater.*, 2025, **35**, 2425244.
121 Q. Shao and S. Jiang, *Adv. Mater.*, 2015, **27**, 15–26.
122 W. Ji, M. Liu, Y. Li, L. Liu, Y. Wang, F. Duan, C. Su, H. Li, R. Cao, J. Yin, M. Wei, Z. Jiang and H. Cao, *Small*, 2024, **20**, 2405113.
123 S. Xue, X. Ma, Y. Wang, G. Duan, C. Zhang, K. Liu and S. Jiang, *Coord. Chem. Rev.*, 2024, **504**, 215659.
124 T. Sun, Z. Wang, Y. Wang, Q. Xu, K. Wang and J. Jiang, *Angew. Chem., Int. Ed.*, 2025, **64**, e202422814.
125 Y. Wang, S. Yang, J. Zhang, Z. Chen, B. Zhu, J. Li, S. Liang, Y. Bai, J. Xu, D. Rao, L. Dong, C. Zhang and X. Yang, *Nat. Commun.*, 2023, **14**, 1108.
126 Y. Zhao, X. Tao, B. Xu, W. Liu and S. Lin, *Adv. Funct. Mater.*, 2024, **34**, 2401895.
127 Z. Miao, G. Liu, Y. Cui, Z. Liu, J. Li, F. Han, Y. Liu, X. Sun, X. Gong, Y. Zhai, Y. Zhao and Y. Zeng, *Angew. Chem., Int. Ed.*, 2019, **58**, 4906–4910.
128 G. Zhang, M. Tsujimoto, D. Packwood, N. T. Duong, Y. Nishiyama, K. Kadota, S. Kitagawa and S. Horike, *J. Am. Chem. Soc.*, 2018, **140**, 2602–2609.
129 C. Qian, Q.-Y. Qi, G.-F. Jiang, F.-Z. Cui, Y. Tian and X. Zhao, *J. Am. Chem. Soc.*, 2017, **139**, 6736–6743.
130 Z. Zhang, A. Xiao, C. Yin, X. Wang, X. Shi and Y. Wang, *Chem. Commun.*, 2022, **58**, 7136–7139.
131 T. H. Lee, M. Balcik, Z. Ali, T. Joo, M. P. Rivera, I. Pinnau and Z. P. Smith, *Science*, 2025, **388**, 839–844.
132 J. Maschita, T. Banerjee and B. V. Lotsch, *Chem. Mater.*, 2022, **34**, 2249–2258.
133 D. N. Bunck and W. R. Dichtel, *Chem. Commun.*, 2013, **49**, 2457–2459.
134 Q.-P. Zhang, Y.-l. Sun, G. Cheng, Z. Wang, H. Ma, S.-Y. Ding, B. Tan, J.-h. Bu and C. Zhang, *Chem. Eng. J.*, 2020, **391**, 123471.
135 B. Gui, X. Liu, Y. Cheng, Y. Zhang, P. Chen, M. He, J. Sun and C. Wang, *Angew. Chem., Int. Ed.*, 2022, **61**, e202113852.
136 X. Jing, M. Zhang, Z. Mu, P. Shao, Y. Zhu, J. Li, B. Wang and X. Feng, *J. Am. Chem. Soc.*, 2023, **145**, 21077–21085.
137 B. F. Hoskins and R. Robson, *J. Am. Chem. Soc.*, 1990, **112**, 1546–1554.
138 O. M. Yaghi and H. Li, *J. Am. Chem. Soc.*, 1995, **117**, 10401–10402.
139 M. Eddaoudi, J. Kim, N. Rosi, D. Vodak, J. Wachter, M. O'Keeffe and O. M. Yaghi, *Science*, 2002, **295**, 469–472.
140 H. Deng, S. Grunder, K. E. Cordova, C. Valente, H. Furukawa, M. Hmadeh, F. Gándara, A. C. Whalley, Z. Liu, S. Asahina, H. Kazumori, M. O'Keeffe, O. Terasaki, J. F. Stoddart and O. M. Yaghi, *Science*, 2012, **336**, 1018–1023.
141 R. Banerjee, H. Furukawa, D. Britt, C. Knobler, M. O'Keeffe and O. M. Yaghi, *J. Am. Chem. Soc.*, 2009, **131**, 3875–3877.
142 S. Cong, Y. Zhou, C. Luo, C. Wang, J. Wang, Z. Wang and X. Liu, *Angew. Chem., Int. Ed.*, 2024, **63**, e202319894.
143 R.-J. Mo, S. Chen, L.-Q. Huang, X.-L. Ding, S. Rafique, X.-H. Xia and Z.-Q. Li, *Nat. Commun.*, 2024, **15**, 2145.
144 Y. Ye, Z. Ma, R.-B. Lin, R. Krishna, W. Zhou, Q. Lin, Z. Zhang, S. Xiang and B. Chen, *J. Am. Chem. Soc.*, 2019, **141**, 4130–4136.
145 Z. Wang and S. M. Cohen, *Angew. Chem., Int. Ed.*, 2008, **47**, 4699–4702.
146 G. Cai and H.-L. Jiang, *Angew. Chem., Int. Ed.*, 2017, **56**, 563–567.
147 D. M. Polyukhov, A. S. Poryvaev, S. A. Gromilov and M. V. Fedin, *Nano Lett.*, 2019, **19**, 6506–6510.
148 D. Mukherjee, S. C. Pal, J.-X. Wang, V. Bon, S. Chand, S. Kaskel, B. Li, D. Volkmer and M. C. Das, *J. Am. Chem. Soc.*, 2025, **147**, 29255–29270.
149 Y. Ying, Z. Zhang, S. B. Peh, A. Karmakar, Y. Cheng, J. Zhang, L. Xi, C. Boothroyd, Y. M. Lam, C. Zhong and D. Zhao, *Angew. Chem., Int. Ed.*, 2021, **60**, 11318–11325.
150 O. Karagiaridi, W. Bury, E. Tylianakis, A. A. Sarjeant, J. T. Hupp and O. K. Farha, *Chem. Mater.*, 2013, **25**, 3499–3503.
151 Z. Han, K. Wang, H. Min, J. Xu, W. Shi and P. Cheng, *Angew. Chem., Int. Ed.*, 2022, **61**, e202204066.
152 N. Wang, A. Mundstock, Y. Liu, A. Huang and J. Caro, *Chem. Eng. Sci.*, 2015, **124**, 27–36.
153 H. Fan, A. Mundstock, J. Gu, H. Meng and J. Caro, *J. Mater. Chem. A*, 2018, **6**, 16849–16853.
154 H. Fan, A. Mundstock, A. Feldhoff, A. Knebel, J. Gu, H. Meng and J. Caro, *J. Am. Chem. Soc.*, 2018, **140**, 10094–10098.
155 J. Chen, R. Li, S. Liu, W. Li, J. Zhang, X. Wu and J. Wang, *J. Membr. Sci.*, 2024, **694**, 122404.
156 Y. Li, Q. Zhang, Z. Dai, R. Wang, Z. Li, Y. Huang, R. Lai, F. Wei and F. Shao, *Adv. Sci.*, 2025, **12**, 2501580.
157 X. Wang, Q. Wang, J. Li, N. Wang and Q.-F. An, *J. Membr. Sci.*, 2024, **691**, 122262.
158 M. Wu, Y. Sun, T. Ji, K. Yu, L. Liu, Y. He, J. Yan, S. Meng, W. Hu, X. Fan, D. Du and Y. Liu, *J. Membr. Sci.*, 2023, **686**, 122023.
159 H. Fan, J. Gu, H. Meng, A. Knebel and J. Caro, *Angew. Chem., Int. Ed.*, 2018, **57**, 4083–4087.
160 H. Fan, M. Peng, I. Strauss, A. Mundstock, H. Meng and J. Caro, *J. Am. Chem. Soc.*, 2020, **142**, 6872–6877.
161 Y. Zhang, J. Guo, G. Han, Y. Bai, Q. Ge, J. Ma, C. H. Lau and L. Shao, *Sci. Adv.*, 2021, **7**, eabe8706.
162 C. Ding, M. Breunig, J. Timm, R. Marschall, J. Senker and S. Agarwal, *Adv. Funct. Mater.*, 2021, **31**, 2106507.

163 Z. Wang, Z. Si, D. Cai, G. L. Shufeng Li and P. Qin, *J. Membr. Sci.*, 2020, **615**, 118466.

164 L. Liu, L. Yin, D. Cheng, S. Zhao, H.-Y. Zang, N. Zhang and G. Zhu, *Angew. Chem., Int. Ed.*, 2021, **60**, 14875–14880.

165 R. Wang, X. Shi, A. Xiao, W. Zhou and Y. Wang, *J. Membr. Sci.*, 2018, **566**, 197–204.

166 R. Wang, M. Wei and Y. Wang, *J. Membr. Sci.*, 2020, **604**, 118090.

167 J. Shen, R. Zhang, Y. Su, B. Shi, X. You, W. Guo, Y. Ma, J. Yuan, F. Wang and Z. Jiang, *J. Mater. Chem. A*, 2019, **7**, 18063–18071.

168 W. Baoyu, Z. Shiyu, L. Zhe, D. Cuiting, D. Hao, Z. Yu, D. Rui, Z. Runnan, Z. Sui and J. Zhongyi, *Small*, 2025, **21**, 2500927.

169 T. Wu, Y. Qian, Z. Zhu, W. Yu, L. Zhang, J. Liu, X. Shen, X. Zhou, T. Qian and C. Yan, *Adv. Mater.*, 2025, **37**, 2415509.

170 Y. Tang, S. Feng, L. Fan, J. Pang, W. Fan, G. Kong, Z. Kang and D. Sun, *Sep. Purif. Technol.*, 2019, **223**, 10–16.

171 S. Chandra, S. Kandambeth, B. P. Biswal, B. Lukose, S. M. Kunjir, M. Chaudhary, R. Babarao, T. Heine and R. Banerjee, *J. Am. Chem. Soc.*, 2013, **135**, 17853–17861.

172 T. Huang, H. Jiang, J. C. Douglin, Y. Chen, S. Yin, J. Zhang, X. Deng, H. Wu, Y. Yin, D. R. Dekel, M. D. Guiver and Z. Jiang, *Angew. Chem., Int. Ed.*, 2023, **62**, e202209306.

173 L. Cao, H. Wu, Y. Cao, C. Fan, R. Zhao, X. He, P. Yang, B. Shi, X. You and Z. Jiang, *Adv. Mater.*, 2020, **32**, 2005565.

174 Z. Zhu, H. Wang, C. Ling, Y. Zhang, J. Zhao, Y. Wang, J. Zhao, F. Pan, C. Wang and Z. Jiang, *Small*, 2024, **20**, 2401172.

175 Y. Zheng, Z. Li, Z. Yang, J. Shen, C. Yang, H. Wang, K. Xu, L. Cheng, Y. Hu, Y. Zhao, R. Zhang and Z. Jiang, *Small*, 2024, **20**, 2403300.

176 J. Wang, X. Zhang, R. Shen, Q. Yuan and Y. Yang, *ACS Nano*, 2024, **18**, 34698–34707.

177 G. M. Geise, *Science*, 2021, **371**, 31–32.

178 Z. Tan, S. Chen, X. Peng, L. Zhang and C. Gao, *Science*, 2018, **360**, 518–521.

179 C. Liu, C.-Y. Zhu, C. Zhang, H.-C. Yang and Z.-K. Xu, *Prog. Polym. Sci.*, 2024, **152**, 101815.

180 X. Wu, T. Chen, G. Dong, M. Tian, J. Wang, R. Zhang, G. Zhang, J. Zhu and Y. Zhang, *Desalination*, 2024, **577**, 117379.

181 D. Chen, J. Sha, X. Mei, A. Ye, Z. Zhao, X. Qiu, X. Liu, Y. Niu, P. Zuo and Q. Zhuang, *Nat. Commun.*, 2024, **15**, 10864.

182 M. Matsumoto, L. Valentino, G. M. Stiehl, H. B. Balch, A. R. Corcos, F. Wang, D. C. Ralph, B. J. Mariñas and W. R. Dichtel, *Chem*, 2018, **4**, 308–317.

183 Y.-A. Wang, Q. Wu, X. Wang, M. Jiang, R. Zhang, X.-J. Chen, R.-P. Liang and J.-D. Qiu, *Angew. Chem., Int. Ed.*, 2024, **63**, e202413071.

184 J. Du, Q. Sun, W. He, L. Liu, Z. Song, A. Yao, J. Ma, D. Cao, S. U. Hassan, J. Guan and J. Liu, *Adv. Mater.*, 2023, **35**, 2300975.

185 A. Ben-Zvi, U. Taqui Syed, G. Z. Ramon and S. Nunes, *Green Chem.*, 2024, **26**, 6237–6260.

186 Y. Pan, H. Liu, Z. Huang, W. Zhang, H. Gao, L. Liang, L. Dong and H. Meng, *Angew. Chem., Int. Ed.*, 2023, **63**, e202316315.

187 H. Wang, J. Zhao, Y. Li, Y. Cao, Z. Zhu, M. Wang, R. Zhang, F. Pan and Z. Jiang, *Nano-Micro Lett.*, 2022, **14**, 216.

188 M. Wang, Y. Wang, J. Zhao, J. Zou, X. Liang, Z. Zhu, J. Zhu, H. Wang, Y. Wang, F. Pan and Z. Jiang, *Angew. Chem., Int. Ed.*, 2023, **62**, e202219084.

189 Y. Liu, Z. Ng, E. A. Khan, H.-K. Jeong, C.-b. Ching and Z. Lai, *Microporous Mesoporous Mater.*, 2009, **118**, 296–301.

190 M. C. McCarthy, V. Varela-Guerrero, G. V. Barnett and H.-K. Jeong, *Langmuir*, 2010, **26**, 14636–14641.

191 X. Liu, C. Wang, B. Wang and K. Li, *Adv. Funct. Mater.*, 2017, **27**, 1604311.

192 H. Guo, G. Zhu, I. J. Hewitt and S. Qiu, *J. Am. Chem. Soc.*, 2009, **131**, 1646–1647.

193 H. Lee, S. M. Dellatore, W. M. Miller and P. B. Messersmith, *Science*, 2007, **318**, 426–430.

194 A. Xie, J. Cui, J. Yang, Y. Chen, J. Lang, C. Li, Y. Yan and J. Dai, *Sep. Purif. Technol.*, 2020, **236**, 116273.

195 A. Huang, Q. Liu, N. Wang and J. Caro, *J. Mater. Chem. A*, 2014, **2**, 8246–8251.

196 A. Huang, H. Bux, F. Steinbach and J. Caro, *Angew. Chem., Int. Ed.*, 2010, **49**, 4958–4961.

197 P. Neelakanda, E. Barankova and K.-V. Peinemann, *Microporous Mesoporous Mater.*, 2016, **220**, 215–219.

198 M. Zhai, F. Moghadam, T. Gosiamemang, J. Y. Y. Heng and K. Li, *Nat. Commun.*, 2024, **15**, 10264.

199 J. Yuan, W.-S. Hung, H. Zhu, K. Guan, Y. Ji, Y. Mao, G. Liu, K.-R. Lee and W. Jin, *J. Membr. Sci.*, 2019, **572**, 20–27.

200 J. Gascon, S. Aguado and F. Kapteijn, *Microporous Mesoporous Mater.*, 2008, **113**, 132–138.

201 J. Wu, Q. Dai, H. Zhang and X. Li, *Energy Storage Mater.*, 2021, **35**, 687–694.

202 J. Yao, D. Dong, D. Li, L. He, G. Xu and H. Wang, *Chem. Commun.*, 2011, **47**, 2559–2561.

203 Y. Zhou, X.-F. Zhang, J. Yao and H. Wang, *Sep. Purif. Technol.*, 2022, **300**, 121837.

204 E. Shamsaei, X. Lin, Z.-X. Low, Z. Abbasi, Y. Hu, J. Z. Liu and H. Wang, *ACS Appl. Mater. Interfaces*, 2016, **8**, 6236–6244.

205 H. T. Kwon and H.-K. Jeong, *J. Am. Chem. Soc.*, 2013, **135**, 10763–10768.

206 C. Zhao, F. Feng, J. Hou, J. Hu, Y. Su, J. Z. Liu, M. Hill, B. D. Freeman, H. Wang and H. Zhang, *J. Am. Chem. Soc.*, 2024, **146**, 14058–14066.

207 J. Wang, Y. Ren, Y. Wang, Z. Li, Z. Song, Q. Zhao, M. Zhao, H. Liu, H. Ma, J. Wang, Y. Dong, Y. Li, G. He and Z. Jiang, *Angew. Chem., Int. Ed.*, 2025, **64**, e202502862.

208 S. Zhou, O. Shekhah, A. Ramírez, P. Lyu, E. Abou-Hamad, J. Jia, J. Li, P. M. Bhatt, Z. Huang, H. Jiang, T. Jin, G. Maurin, J. Gascon and M. Eddaoudi, *Nature*, 2022, **606**, 706–712.

209 Y. Peng, Y. Li, Y. Ban and W. Yang, *Angew. Chem., Int. Ed.*, 2017, **56**, 9757–9761.

210 M. Qiu, Z. Zhu, D. Wang, Z. Xu, F. Xia, L. Jiang and Y. Tian, *Adv. Funct. Mater.*, 2024, **34**, 2316040.

211 S. S. Ray, S.-S. Chen, D. Sangeetha, H.-M. Chang, C. N. D. Thanh, Q. H. Le and H.-M. Ku, *Environ. Chem. Lett.*, 2018, **16**, 1247–1265.

212 J. R. Werber, C. O. Osuji and M. Elimelech, *Nat. Rev. Mater.*, 2016, **1**, 16018.

213 L. Long, C. Wu, S. Shao, Z. Yang, P. Sarkar and C. Y. Tang, *Nat. Water*, 2025, **3**, 668–682.

214 S. Dutta, R. F. de Luis, J. Goscianska, A. Demessence, R. Ettlinger and S. Wuttke, *Adv. Funct. Mater.*, 2024, **34**, 2304790.

215 M. Jian, R. Qiu, Y. Xia, J. Lu, Y. Chen, Q. Gu, R. Liu, C. Hu, J. Qu, H. Wang and X. Zhang, *Sci. Adv.*, 2020, **6**, eaay3998.

216 S.-H. Li, H. Mao, Y.-N. Feng, L.-H. Xu, H. Qi and Z.-P. Zhao, *Nat. Commun.*, 2025, **16**, 7404.

217 M. Wang, P. Zhang, X. Liang, J. Zhao, Y. Liu, Y. Cao, H. Wang, Y. Chen, Z. Zhang, F. Pan, Z. Zhang and Z. Jiang, *Nat Sustain*, 2022, **5**, 518–526.

218 Q. Sun, J. Du, A. Yao, Y. Zhang, B. Yu, W. Lim, S. U. Hassan, J. Guan, P. Dou and J. Liu, *ACS Nano*, 2025, **19**, 18409–18420.

219 Y. Zheng, Z. Yang, Z. Li, W. Liu, C. Yang, J. Shen, H. Wang, K. Xu, L. Cheng, R. Zhang and Z. Jiang, *J. Membr. Sci.*, 2025, **713**, 123363.

220 S. Yang, Y. Wang, H. Pan, P. He and H. Zhou, *Nature*, 2024, **636**, 309–321.

221 L. Zhou, S. Gu, S. Li and Z. Xu, *Adv. Funct. Mater.*, 2025, 2506147.

222 Q.-W. Meng, X. Zhu, W. Xian, S. Wang, Z. Zhang, L. Zheng, Z. Dai, H. Yin, S. Ma and Q. Sun, *Proc. Natl. Acad. Sci.*, 2024, **121**, e2316716121.

223 L. Ren, J. Chen, J. Han, J. Liang and H. Wu, *Chem. Eng. J.*, 2023, **462**, 142112.

224 T. Dang, Z.-Y. Zhang and T. Li, *J. Am. Chem. Soc.*, 2024, **146**, 19609–19620.

225 L. Ren, J. Chen, J. Han, J. Liang and H. Wu, *Chem. Eng. J.*, 2024, **482**, 148907.

226 V. Balaram, *Geosci. Front.*, 2019, **10**, 1285–1303.

227 J. Kujawa, S. Al Gharabli, A. Szymczyk, A. P. Terzyk, S. Boncel, K. Knozowska, G. Li and W. Kujawski, *Coord. Chem. Rev.*, 2023, **493**, 215340.

228 X. Shi, X. Wang, T. Feng, T. Ju, J. Long, C. Yin, Z. Zhang and Y. Wang, *J. Membr. Sci.*, 2024, **712**, 123240.

229 B. Zheng, J. Fan, B. Chen, X. Qin, J. Wang, F. Wang, R. Deng and X. Liu, *Chem. Rev.*, 2022, **122**, 5519–5603.

230 P. Chatterjee, A. Volkov, J. Mi, M. Niu, S. Sun, A. J. Rossini, L. M. Stanley and W. Huang, *J. Am. Chem. Soc.*, 2024, **146**, 20468–20476.

231 C. Deng, J. Zhang, Y. Zou, Y. Zhang, N. He, J. Zhou, Y. Li, L. Zhao and L. Ma, *Sep. Purif. Technol.*, 2025, **360**, 131120.